Molecular Cell

Article

Transcription activation is enhanced by multivalent interactions independent of phase separation

Graphical abstract

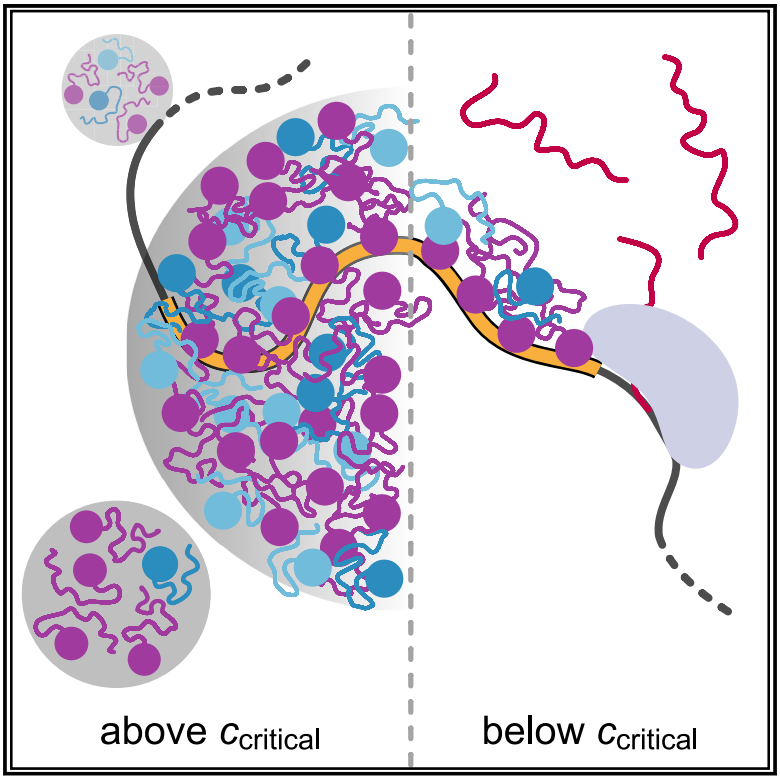

Authors

Jorge Trojanowski, Lukas Frank, Anne Rademacher, Norbert Mücke, Pranas Grigaitis, Karsten Rippe

Correspondence

karsten.rippe@dkfz.de

In brief

Phase separation of TFs into condensates has been proposed to enhance transcription activation. Trojanowski et al. show that a high propensity of TFs to engage in multivalent interactions is needed for their full activation capacity independent of TF assembly into phase-separated liquid-like droplets.

Highlights

- Strongly activating TFs have a high propensity to engage in multivalent interactions
- Formation of liquid-like TF droplets does not enhance transcription activation
- Longer TF residence time increases transcription independent of site occupancy
- High TF multivalency promotes recruitment of transcription coactivators

Trojanowski et al., 2022, Molecular Cell *82*, 1878–1893
May 19, 2022
https://doi.org/10.1016/j.molcel.2022.04.017

CellPress

CellPress

Molecular Cell

Article

Transcription activation is enhanced by multivalent interactions independent of phase separation

Jorge Trojanowski,[1,3] Lukas Frank,[1,3] Anne Rademacher,[1] Norbert Mücke,[1] Pranas Grigaitis,[1,2] and Karsten Rippe[1,4,*]
[1]Division of Chromatin Networks, German Cancer Research Center (DKFZ) and Bioquant, Heidelberg, Germany
[2]Present address: Systems Biology Lab, Amsterdam Institute of Molecular and Life Sciences, AIMMS), Amsterdam, the Netherlands
[3]These authors contributed equally
[4]Lead contact
*Correspondence: karsten.rippe@dkfz.de
https://doi.org/10.1016/j.molcel.2022.04.017

SUMMARY

Transcription factors (TFs) consist of a DNA-binding domain and an activation domain (AD) that are frequently considered to be independent and exchangeable modules. However, recent studies report that the physicochemical properties of the AD can control TF assembly at chromatin by driving phase separation into transcriptional condensates. Here, we dissected transcription activation by comparing different synthetic TFs at a reporter gene array with real-time single-cell fluorescence microscopy. In these experiments, binding site occupancy, residence time, and coactivator recruitment in relation to multivalent TF interactions were compared. While phase separation propensity and activation strength of the AD were linked, the actual formation of liquid-like TF droplets had a neutral or inhibitory effect on transcription activation. We conclude that multivalent AD-mediated interactions enhance the transcription activation capacity of a TF by increasing its residence time in the chromatin-bound state and facilitating the recruitment of coactivators independent of phase separation.

INTRODUCTION

The dynamic binding of transcription factors (TFs) and coactivators to promoters and enhancers is central to gene regulation (Lu and Lionnet, 2021; Soto et al., 2022; Wong and Gunawardena, 2020). Most TFs contain a structurally well-defined DNA-binding domain (DBD) and a separate activation domain (AD) that frequently has intrinsically disordered regions (IDRs) (Soto et al., 2022). By combining DBDs and ADs in a modular manner, a number of synthetic TFs have been constructed (Brent and Ptashne, 1985; Chavez et al., 2015; Sadowski et al., 1988). These TFs employ ADs with a particularly high transcription activation capacity like VP16 from a herpes simplex virus protein (Sadowski et al., 1988) and VPR (VP64-p65-Rta), a tripartite synthetic construct that consists of VP64 (four copies of VP16) fused to the p65 and Rta ADs (Chavez et al., 2015). Moreover, it is well established that the TF promoter-binding site occupancy θ and kinetic binding parameters of a given DBD regulate target gene expression (Lu and Lionnet, 2021; Wong and Gunawardena, 2020). The value of θ is determined by the concentration of the free TF and the ratio of the kinetic on- and off-rates for binding: $\theta = [TF]/([TF] + k_{off}/k_{on})$. Thus, binding sites become fully saturated at sufficiently high TF concentrations. However, not only binding site occupancy but also TF residence time as given by $\tau_{res} = 1/k_{off}$ could determine the transcriptional activation capacity (Callegari et al., 2019; Gurdon et al., 2020; Loffreda et al., 2017; Popp et al., 2021; Shelansky and Boeger, 2020). The value of τ_{res} can become rate limiting for a multistep activation process if a TF-binding event with a certain duration is required to drive a subsequent reaction that induces transcription (Wong and Gunawardena, 2020). While these parameters of TF-DNA interactions strongly depend on the DBD, recent studies showed that TF assembly at chromatin is not limited to direct DBD-DNA interactions. The IDRs found in TF ADs of SP1, TAF15, OCT4, β-catenin, STAT3, and SMAD3, in transcriptional coactivators such as MED1/19, p300, and BRD4, and in the unstructured C-terminal domain (CTD) of RNA polymerase II (RNA Pol II) can drive the formation of phase-separated transcriptional condensates at enhancers and promoters (Cho et al., 2018; Han et al., 2020; Hnisz et al., 2017; Ma et al., 2021; Sabari, 2020; Sabari et al., 2018; Shrinivas et al., 2019; Soto et al., 2022; Wei et al., 2020; Zhang et al., 2021). One mechanism frequently invoked for this process is liquid-liquid phase separation (LLPS). Above a critical or saturating concentration (c_{crit}), multivalent interactions of proteins and RNAs that frequently involve IDRs drive the formation of phase-separated liquid-like droplets that sequester their constituting components from the surrounding nucleoplasm (Banani et al., 2017; Choi

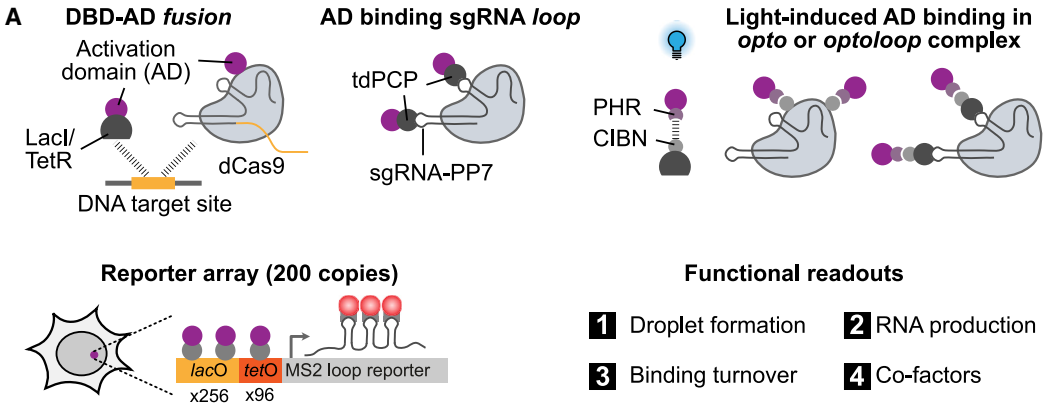

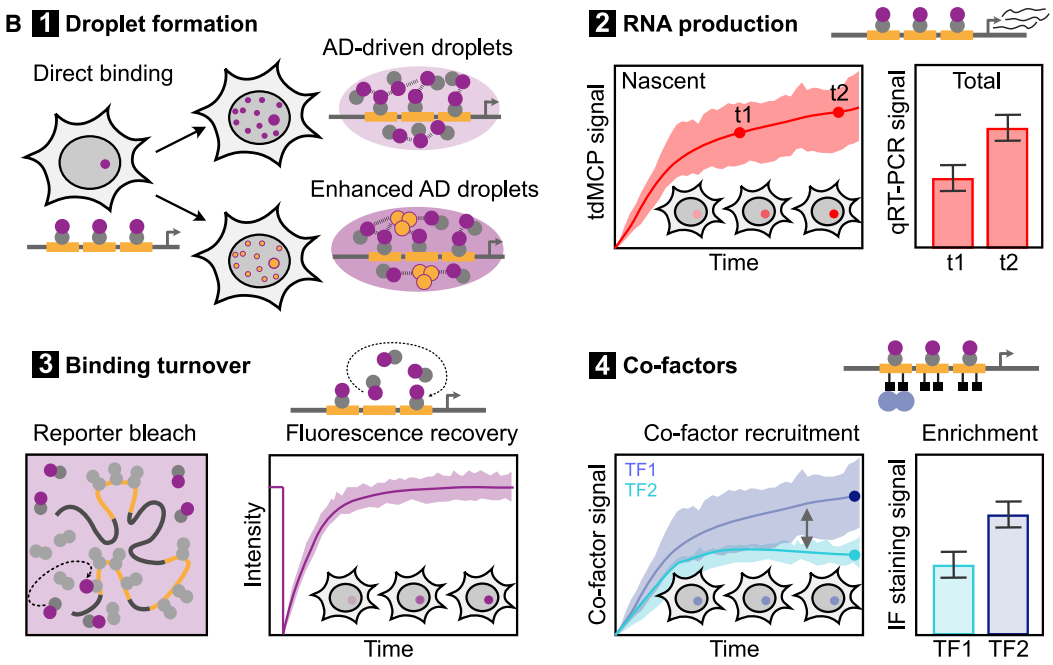

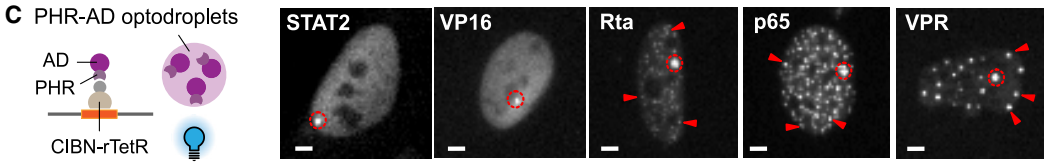

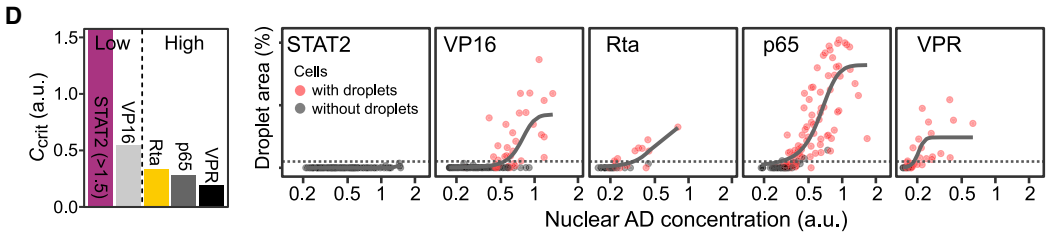

(legend on next page)

et al., 2020; Shin and Brangwynne, 2017). This type of TF assembly could enhance transcription by different mechanisms that include (1) increasing the local TF concentration at the promoter, (2) mediating the recruitment of coactivators and/or additional RNA Pol II complexes, and (3) accelerating TF target search (Hnisz et al., 2017; Mazzocca et al., 2021; Sabari, 2020; Schneider et al., 2021; Shrinivas et al., 2019; Wei et al., 2020). However, the assembly of chromatin subcompartments could be governed by alternative mechanisms including classical (cooperative) chromatin binding, formation of specific multisubunit protein complexes, and bridging interactions between distant binding sites (Erdel and Rippe, 2018; McSwiggen et al., 2019; Rippe, 2022; Rippe and Papantonis, 2022). Furthermore, current studies lack a comparison of a TF in the droplet state to the same TF bound to chromatin but without droplet formation, which is crucial to assess the functional role of transcriptional condensates for gene activation.

Here, we have studied a panel of synthetic TF constructs with different DBDs and ADs. We evaluated these TFs with respect to their binding interactions and activation capacity by fluorescence microscopy and assessed the contribution of liquid droplet formation. Striking differences in chromatin-bound residence time, RNA production, histone H3 acetylation at lysine 27 (H3K27ac), and BRD4 recruitment between different TF constructs were observed. Furthermore, we link the phase separation propensity of the AD to TF-DNA-binding properties and activation capacity. Based on our results, we conclude that the ability of a TF to engage in multivalent interactions enhances its activation strength. However, we find no evidence that the formation of liquid droplets per se would enhance transcription.

RESULTS

TF properties affecting transcription initiation are dissected with modular constructs

We generated a toolbox of single- and multicomponent TF constructs and applied them to study transcriptional activation in the human U2OS 2-6-3 reporter cell line (Janicki et al., 2004) (Figure 1A; Tables S1 and S2). The cell line contains *lac*O and *tet*O repeats followed by a CMV core promoter and an inducible reporter gene with MS2 sequences. This setup enables time-resolved measurements of TF binding in single living cells. Furthermore, nascent RNA production can be visualized by the binding of fluorescently tagged MS2 coat protein (tdMCP) to the MS2 RNA (Pankert et al., 2017). The three DBDs employed to target the reporter were reverse *tet* repressor (rTetR, DNA binding in the presence of doxycycline), *lac* repressor (LacI), and dead-Cas9 (dCas9) with single-guide RNAs (sgRNA) targeting *lac*O or *tet*O sites (Table S3). ADs were linked to these DBDs via four different approaches (Figure 1A; Table S1): protein fusion, binding of PP7 coat protein (tdPCP) AD fusions to PP7 RNA loops (Zalatan et al., 2015) in the sgRNA (“loop”), light-induced binding by heterodimer formation between PHR-AD and DBD-CIBN fusion proteins (“opto”) (Kennedy et al., 2010; Rademacher et al., 2017) as well as complexes formed by a PP7-sgRNA, tdPCP-CIBN, and PHR-AD constructs (“opto-loop”). The CIBN-dCas9-CIBN (“dCas9-opto”) construct has previously been used in the LACE system (Polstein and Gersbach, 2015). As expected, TF complexes from this toolbox bound the reporter gene array (Figure S1A). Light-induced complexes accumulated the AD within seconds upon illumination (Figure S1B) and induced RNA production (Figures S1C and S1D). In this manner, transcription initiation could be dissected at high temporal resolution in living cells as reported previously (Rademacher et al., 2017).

We investigated TF properties with respect to four main functional readouts (Figure 1B): (1) the effect of phase-separated TF droplet formation was evaluated with the opto complexes that are based on the light-controlled PHR/CIBN domains for fast and reversible TF accumulation. The increased self-association of PHR constructs upon blue light illumination into optodroplets provides a model system for phase-separated TFs (Shin et al., 2017)(Bracha et al., 2018). This property can be tuned by the PHR fusion partner or reinforced by increasing the binding valency (Erdel et al., 2020). (2) The kinetics of nascent RNA synthesis were traced via tdMCP binding to the MS2 RNA, while the total reporter RNA produced was quantitated by quantitative reverse transcription PCR (qRT-PCR). (3) The residence times of the TF constructs were measured by fluorescence recovery after photobleaching (FRAP) of fluorescent TF molecules accumulating at the reporter’s binding site cluster. (4) The enrichment of two transcription activation marks, H3K27ac and BRD4 binding, was recorded at the reporter array.

PHR-TFs form phase-separated assemblies depending on their AD fusion partner

Optodroplet formation can be exploited to evaluate the phase separation propensity of proteins in living cells (Erdel et al., 2020; Shin et al., 2017). Using our light-inducible TF system, we investigated droplet formation of PHR fusions with five previously described ADs (VP16, p65, Rta, STAT2, and VPR) (Figures 1C and S2A; Table S2). Above a critical concentration

Figure 1. A modular transcription factor toolbox for analysis of transcription activation

(A) DNA-binding domains (DBDs) were combined with different ADs as direct fusions, via binding of PP7 coat protein (tdPCP) to PP7 RNA loops in the sgRNA (“loop”) or fused to the PHR domain for light-induced interactions with CIBN modules (“opto/optoloop”).

(B) The TF activity in the reporter cell line was analyzed with different readouts: (1) droplet formation by light-inducible PHR-AD interactions. (2) Fluorescent readout of nascent RNA or endpoints by qRT-PCR. (3) TF-binding turnover at *tet*O/*lac*O-binding sites by FRAP. (4) TF-triggered enrichment of cofactors measured by microscopy.

(C) GFP-tagged ADs fused to PHR revealed different propensities for droplet formation (arrows) upon light stimulation in addition to the accumulation at the reporter array (dashed circle). Scale bar, 5 μm.

(D) Determination of c_{crit}. The droplet area percentage in the nucleus was plotted against the AD concentration as given by the nuclear intensity of the GFP signal. Cells were classified by visual inspection as droplet positive (red) or negative (gray). Then c_{crit} was determined from the intersection of the logistic fit function and the threshold (dashed line). The resulting values for c_{crit} are shown in the bar plot to the right that assigns ADs into low (STAT2 and VP16) or high (Rta, p65, and VPR) phase separation propensity.

c_{crit}, optodroplets were detectable as nuclear spots outside the reporter array. The relatively high mobility of these ectopic AD assemblies indicates that they were not bound to chromatin. They had properties of liquid droplets as inferred from the fast exchange with the nucleoplasm measured by FRAP and the occurrence of droplet fusion events (Figures S2B and S2C). Rta, p65, and VPR readily assembled into droplets, whereas they were rare or absent for VP16 and STAT2. We quantified the propensity to undergo this process by determining the fraction of cells with visible droplets, which ranged from <1% (STAT2) and 29% (VP16) to 41% (Rta), 72% (p65), and 86% (VPR) (Figure 1C; Table S4). In addition, we determined the area of droplets relative to the nuclear area in dependence of the concentration (Figure 1D). From this relationship, we derived c_{crit} for droplet formation as the nuclear fluorescence signal at which the relative droplet area crossed an empirically defined threshold. Thus, c_{crit} describes the propensity of the AD to drive phase separation. The c_{crit} values (in arbitrary fluorescence intensity units) ranged from 0.19 for VPR to 0.54 (VP16) and >1.5 (STAT2) (Figure 1D; Table S4) and distinguished ADs with high (Rta, p65, and VPR) or with low (STAT2 and VP16) LLPS propensity. Furthermore, the value of c_{crit} defined the concentration where a given PHR-AD construct would be either in the dispersed state (below c_{crit}) or undergo LLPS (above c_{crit}). Thus, LLPS-specific features can be identified by comparing the same AD at expression levels below or above c_{crit} and using the presence/absence of ectopic droplets as a proxy for these two concentration regimes.

Reporter-bound PHR-TFs can accumulate in subdomains with liquid-like properties

We asked whether an activator concentration above c_{crit} also affected AD assembly at the reporter array. We observed that under these conditions PHR-AD constructs accumulated much more strongly and in a granular pattern (Figure 2A). The subdomains that formed above c_{crit} resembled droplets in their shape and size and were able to coalesce with neighboring ones as well as with droplets outside of the array, indicative of a liquid-like state (Figure 2B; Videos S1, S2, and S3). However, apart from fusion events, exchange between these subdomains did not occur on the minute timescale as apparent from FRAP experiments that evaluated the exchange between a bleached and nonbleached part of the reporter array (Figure S2D). Super-resolution radial fluctuation (SRRF) microscopy (Gustafsson et al., 2016) of PHR-VPR at the locus above/below c_{crit} confirmed that the cluster did not assemble into a single homogeneous droplet but contains multiple regions with AD enrichment (Figure 2C). Direct stochastic optical reconstruction microscopy (dSTORM) (Heilemann et al., 2008) additionally revealed binding at multiple distinct sites along the gene array in cells without droplets, which likely represents individual *tetO* repeat units (Figure 2D). In cells with droplets, the AD signal occupied a larger region with multiple sites of local enrichment. Furthermore, PHR-VPR had a 3.6-fold higher intensity at the locus and covered a larger area (3.6 versus 3.2 μm^2) above c_{crit} that extended beyond the *lacO* repeats marked by LacI (Figures 2E and 2F). Next, we pre-exposed the cells to blue light for 60–120 s to saturate the direct binding of PHR-VPR to rTetR-opto at the gene array. Subsequently, a 10-min image series was acquired to monitor the binding of VPR. No further recruitment was observed below c_{crit}, which is consistent with kinetics reported previously for PHR-VP16 (Rademacher et al., 2017) (Figure 2G). However, above c_{crit}, the VPR signal at the reporter array approximately tripled, demonstrating a significant accumulation of indirectly bound protein. Thus, at the ~32-nm localization accuracy of our dSTORM images, the formation of ectopic droplet assemblies outside the reporter array was a proxy for similar processes occurring at the gene array. We conclude that PHR-VPR forms subdomains with liquid-like properties at the reporter locus above c_{crit} that did not display preferential mixing between them.

AD strength is linked to the propensity to undergo phase separation

Phase separation of TFs has been invoked as a mechanism that amplifies RNA Pol II transcription activation (Hnisz et al., 2017; Sabari et al., 2018; Schneider et al., 2021; Shrinivas et al., 2019; Wei et al., 2020). To test this model, we compared ADs with high (p65, Rta, and VPR) versus low (VP16 and STAT2) propensity to form liquid droplets (Figures 1C and 1D; Table S4). We first measured nascent RNA production at the reporter array after light-induced AD recruitment (Figure 3A). We compared the fraction of responding cells, the time to half-maximal activation, and the maximum RNA levels at the end of the 90-min time course. These parameters characterize complementary aspects of the AD transcription activation strength. All five ADs were able to induce transcription but with different strengths (Figures 3B–3D; Tables S4 and S5): (1) p65, Rta, and VPR displayed higher maximum transcription levels (a.u.) of 1.7–2.9 compared with 1.3–1.6 for VP16 and STAT2 ($p < 0.001$, two-way ANOVA) (Figures 3B and S2E) after 90 min. (2) The fraction of responding cells was larger with 67%–92% (p65, Rta, and VPR) versus 42%–67% (VP16 and STAT2) (Figure 3C). (3) The time to reach half-maximal activation was shorter with 26–28 min (p65, Rta, and VPR) compared with 38–42 min (VP16 and STAT2) (Figure S2F; Table S5). We conclude that ADs with a higher phase separation propensity such as p65, Rta, and VPR are stronger activators than VP16 and STAT2 that displayed a low tendency to form droplets.

Phase-separated TF compartments are not required for efficient transcription

Our previous experiments established that PHR-AD constructs assemble into subdomains with liquid-like properties at the gene array above c_{crit}, which is detected by the presence of ectopic droplets (Figure 2). Next, we determined whether the formation of this state enhances transcription activation. Accordingly, the RNA time courses (Figure 3B) were split into cells with and without visible droplets, that is, PHR-AD concentrations above/below c_{crit} Videos S4·S5·S6(Videos S4-S8). The comparison of activation kinetics between the two groups showed no significant differences in the activation rate or the maximum value of RNA production (Figures 3E–3G and S2G; Table S5). Cells with droplets had somewhat higher levels of nascent RNA for VPR, while the opposite trend was observed for cells with droplets for p65 and Rta. However, these differences were not significant ($p > 0.05$ in pairwise t test and two-way

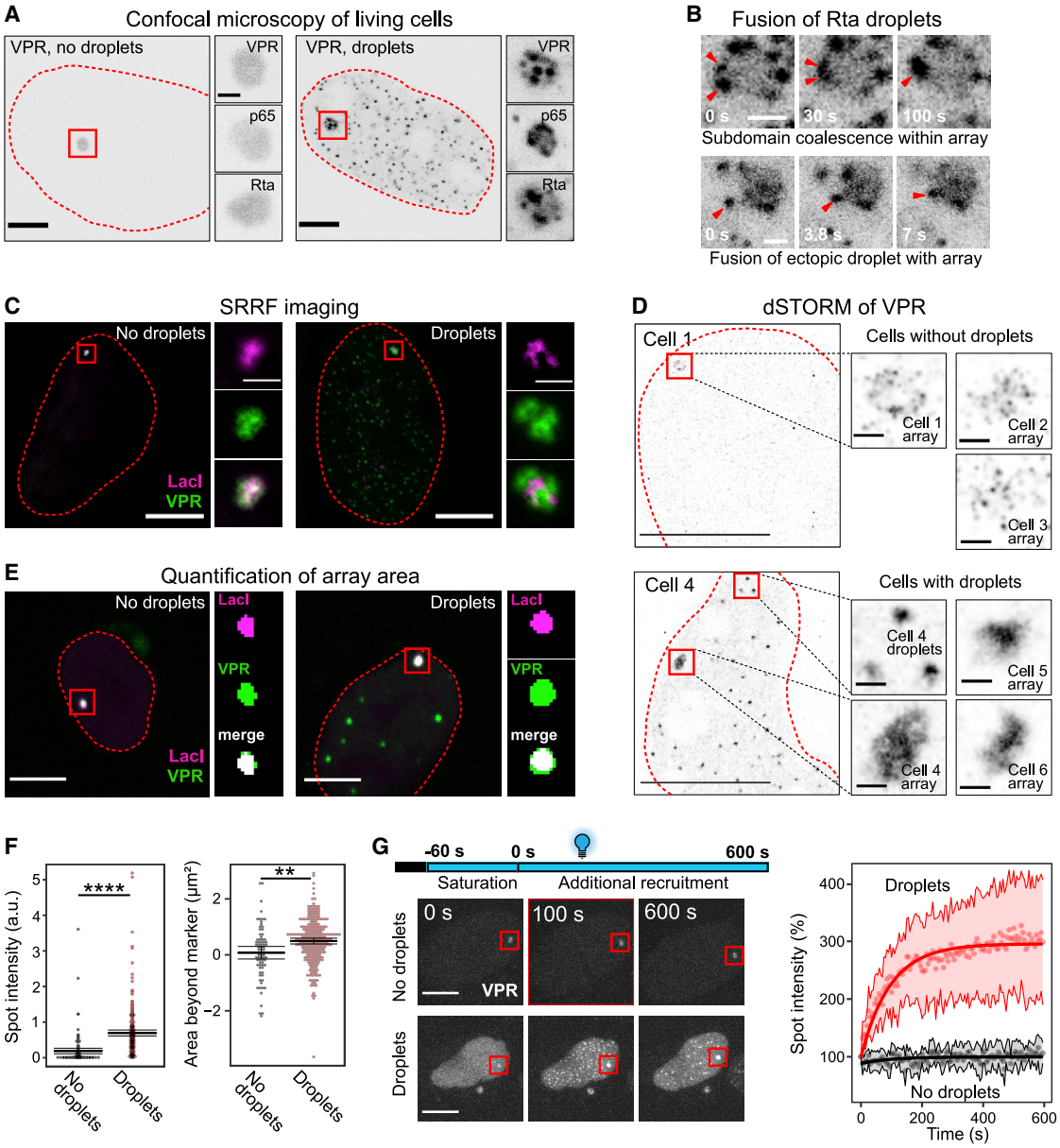

Figure 2. AD organization at reporter gene array above/below c_{crit}

If not stated otherwise, GFP-tagged PHR-AD constructs were recruited by illumination for 10 min to rTetR-opto at the array labeled with tdTomato-LacI.

(A) Live cell confocal microscopy of VPR, p65, and Rta showing much stronger accumulation and formation of granular reporter-bound domains in droplet-containing cells (single z plane). Scale bars, 5 µm (overview) and 1 µm (zoom).

(B) Liquid-droplet-like behavior of reporter-bound domains (top) or ectopic droplets (bottom) for Rta. Scale bar, 1 µm.

(C) SRRF images of VPR and LacI array marker. Scale bars, 10 µm (overview) and 1 µm (zoom).

(D) dSTORM images of fixed cells of PHR-VPR stained with an Alexa 647 conjugated GFP-nanobody in cells without (top) and with (bottom) ectopic droplets. Intensities were linearly adjusted for each individual cell. Scale bars, 10 µm (overview) and 0.5 µm (zoom).

(E) Confocal images of VPR (green) and the LacI array marker (magenta) in fixed cells. Signals were segmented to determine the area covered by VPR versus LacI and the intensities at the array.

(F) Quantification of VPR accumulations at the reporter. The spot intensity was normalized to the LacI marker for cells with (n = 255) or without (n = 121) droplets. The difference between VPR and marker area was quantified for the two states (n = 244 and 73 cells, respectively). VPR displayed a largely increased accumulation at the array in cells with droplets. Two-sided unpaired Welch's t test, $^{**}p < 0.01$; $^{****}p < 0.0001$.

(G) Kinetics of VPR recruitment after pre-illumination to saturate direct binding to rTetR-opto (scheme, top). Subsequent imaging with constant illumination revealed additional recruitment only in cells with droplets. Scale bar, 10 µm. Average spot intensity relative to the start of the imaging time course. 95% CI, n = 7–15.

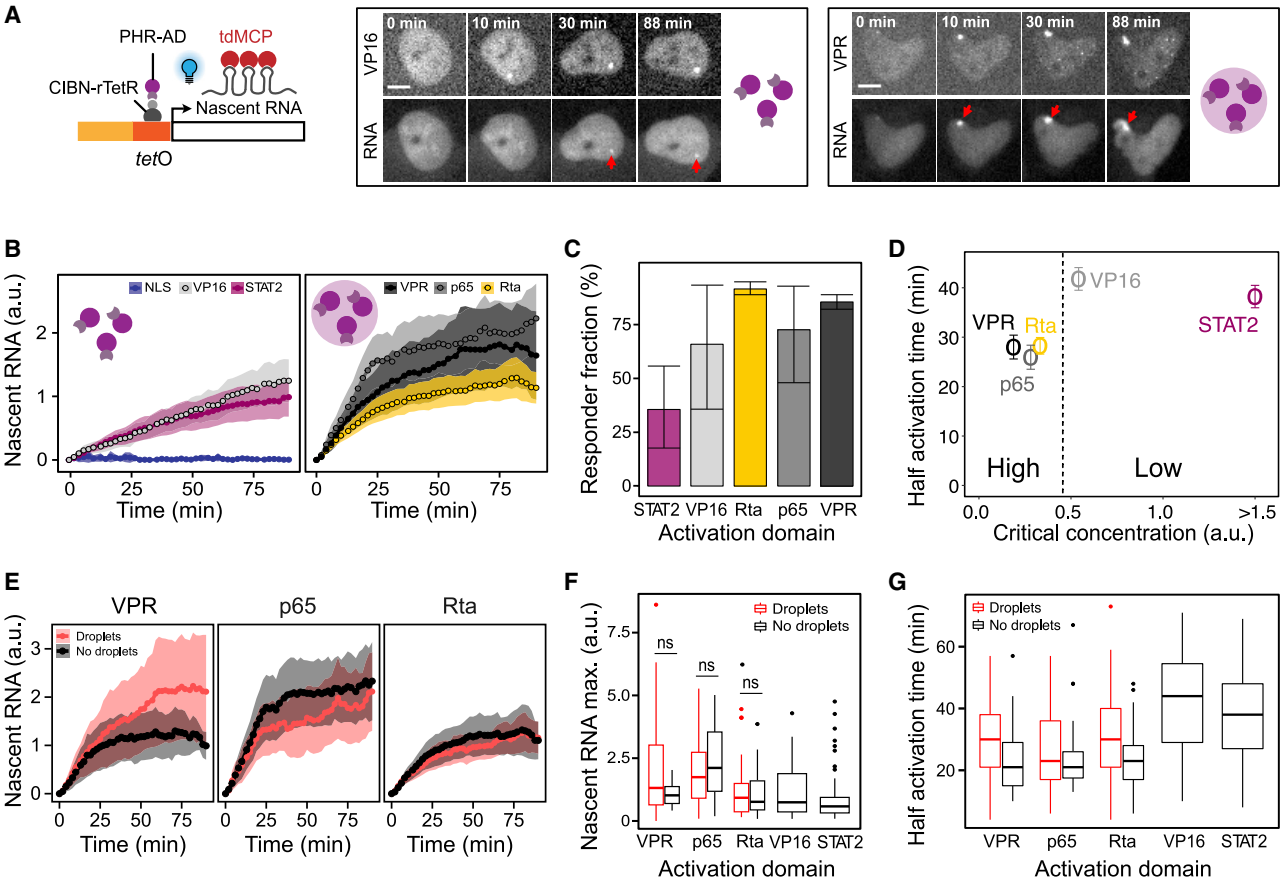

Figure 3. Phase separation of ADs and transcription activation

(A) Experimental approach: GFP-tagged PHR-AD constructs were recruited to the gene array via rTetR-opto upon light illumination. Time courses of nascent RNA and formation of droplets were recorded for ADs with high (VPR) and low (VP16) droplet-forming propensity. Scale bar, 10 μm.

(B) Average nascent RNA kinetics of responding cells for different ADs with mean and 95% CI (n = 31–71 cells per construct). PHR-NLS served as a negative control.

(C) Fraction of cells with visible enrichment of nascent RNA at the reporter. Bars represent mean with minimum and maximum values from 2 to 3 replicates.

(D) Time to half-maximal activation determined from the RNA production kinetics plotted against c_{crit} for ADs with high- and low-phase separation propensity. Error bars represent SEM.

(E) Average nascent RNA time courses of cells visually classified as droplet-positive (red) or -negative (black) with 95% CI (n = 13–18 cells per condition).

(F) Nascent RNA plateau values were calculated from the last 5 time points. For VPR, p65, and Rta cells with or without droplets were compared (n = 13–55 cells per condition, non-responding cells excluded). Unpaired two-sided Welch's t test, $p > 0.05$, not significant (ns).

(G) Time to half-maximal activation of samples described in (F). Transcription activation in droplet-positive cells (above c_{crit}) was indistinguishable or slightly slower as compared to cells with AD concentrations below c_{crit} ($p = 0.09$, two-way ANOVA).

ANOVA). Similarly, changes in the time to half activation for p65 (26 ± 8 min, unchanged), VPR (25 ± 6 to 30 ± 9 min), and Rta (25 ± 4 to 31 ± 5 min) were also not significant ($p > 0.05$, two-way ANOVA accounting for AD type and presence/absence of droplets) (Figures 3G and S2G). We conclude that the accumulation of ADs into droplets did not lead to enhanced transcriptional activation.

To further corroborate this conclusion, we examined the effect of reinforcing droplet formation of VP16 that per se had a low-phase separation propensity (Figure 4). We recruited PHR-VP16 via the rTetR-opto complex but increased its binding valency by additional bridging factors or fusion of a phase separation driving domain. Three approaches were compared: (1) cotransfection of CIBN-LacI as a bridging factor between PHR-VP16 molecules by LacI dimer formation (Lewis et al., 1996) (Figure 4A). (2) Binding of a second PHR domain via PHR fused to GBP (GFP-binding protein), which binds GFP with high affinity (Figure 4B). (3) Fusion of VP16 to the N-terminal IDR of FUS (fused in sarcoma) protein (FUSN) (Figure 4C), which has a high propensity to form liquid droplets *in vitro* and *in vivo* (Patel et al., 2015).

The addition of CIBN-LacI lowered c_{crit} of VP16 (Figure S2A; Table S4) increased the fraction of cells with droplets and increased the local VP16 concentration at the reporter array (Figures 4D and S3C). However, nascent and total reporter RNA levels did not increase, but rather were largely reduced. The fraction of responding cells decreased from 70% to 24% (Figures 4E–4G, S3A, and S3B). Cotransfection of the

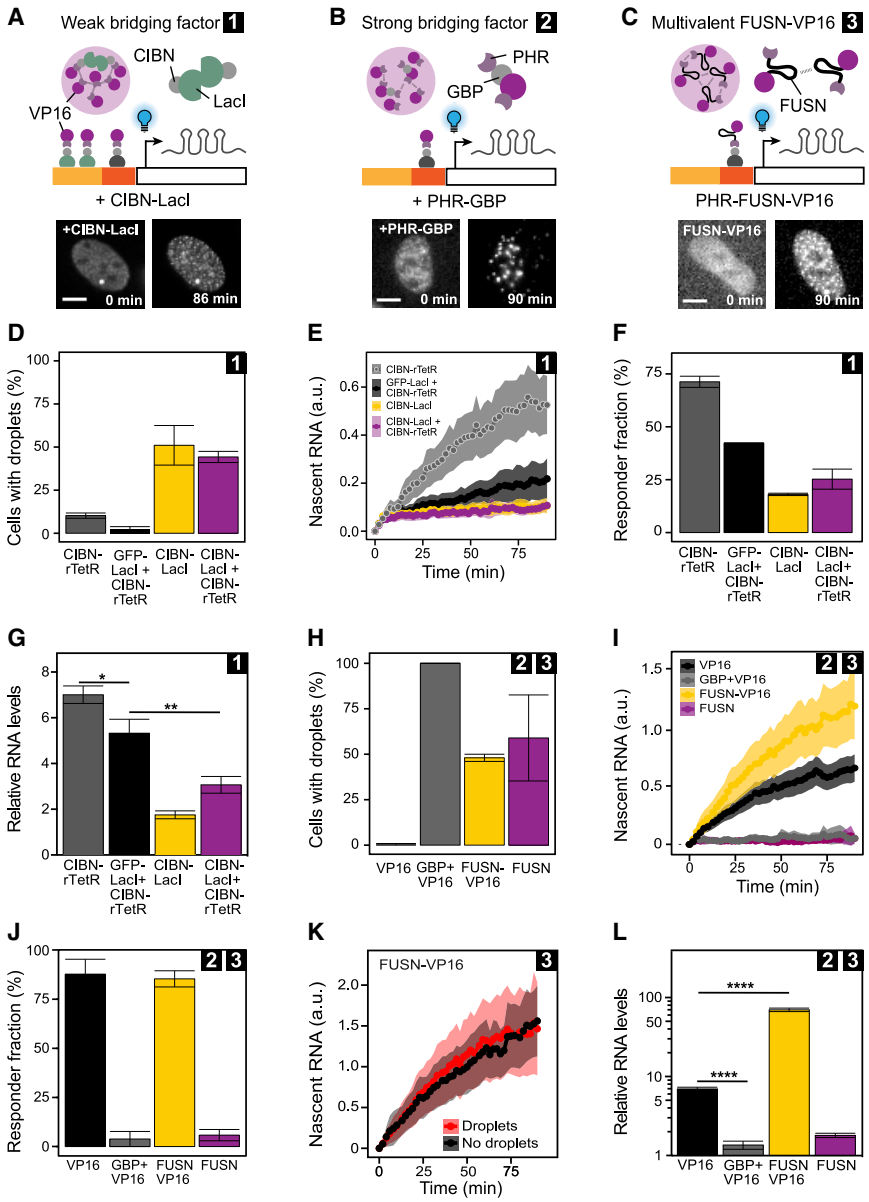

Figure 4. Reporter array activation upon increased droplet formation of VP16

Three different approaches to reinforce droplet formation of PHR-VP16 were implemented (A–C, numbered 1, 2, and 3 for reference in D–L). Light illumination induced droplet formation and binding of VP16 constructs to rTetR-opto at the reporter as illustrated on the images in panels A–C at the beginning and end of the time courses. Scale bar, 10 μm.

(A) Droplet formation by the weak bridging factor CIBN-LacI that also binds to the *lac*O sites.

(B) Droplet formation by PHR-GBP that acts as a strong bridging factor.

(C) Droplet formation by fusion to FUSN.

(D) Fraction of cells with visible VP16 droplets formed in the presence of CIBN-LacI. Bar: mean, error bars: minimum and maximum of two replicates.

(E) Averaged nascent RNA time courses and 95% CI for activation in presence of CIBN-LacI-induced droplets for responding and nonresponding cells combined (n = 74–126 cells per condition).

(F) Fraction of cells with visible enrichment of nascent RNA at the reporter.

(G) Total reporter RNA levels were measured by qRT-PCR at 90 min. Mean and SD of fold-change induction compared with mock-transfected samples and normalized to β-actin mRNA (n = 3). Two-sided unpaired Student's t test compared with mock, *$p < 0.05$, **$p < 0.01$, ****$p < 0.0001$.

(H) Fraction of droplet positive cells for the experimental setup described in (B) and (C).

(I) Averaged nascent RNA time courses and 95% CI for activation in the presence of GBP- or FUSN-induced droplets for responding and non-responding cells combined (n = 24–154 cells per condition).

(J) Fraction of cells with visible enrichment of nascent RNA at the reporter.

(K) Average nascent RNA time courses and 95% CI for responding cells activated by FUSN-VP16 stratified by the presence of droplets (n = 47 cells per condition).

(L) Total reporter RNA levels were measured by qRT-PCR as described for (G).

nonbridging control GFP-LacI revealed some repression but to a much lower extent. Increasing the valency of VP16 via GBP was even more effective in inducing droplet formation (Figures 4B and 4H). Similar to the CIBN-LacI experiment, transcription was repressed as apparent from lower nascent and total reporter RNA levels as well as a strongly reduced responder fraction (Figures 4I–4L and S3D). The use of a (nonbridging) Halotag-GBP control confirmed that transcription inhibition was not caused by direct steric interference of GBP with VP16 (Figures S3J and S3K). Finally, droplet formation of VP16 was increased by fusion to FUSN, which also significantly enhanced transcription activation, while FUSN alone did not activate the reporter (Figures 4C, 4H–4J, and S3D). Total RNA levels were 10-fold higher than those measured for VP16 alone (Figure 4L) with similar RNA activation kinetics (Figure S3E). To test whether the increased activation potential of FUSN-VP16 was related to droplet formation, we again separated the nascent RNA time courses into cells with and without visible droplets (Figure 4K). We found that the activation capacity of FUSN-VP16 was indistinguishable between the two groups. This finding corroborates the results obtained for p65, Rta, and VPR that have high phase separation propensity but displayed no significant change of their activation capacity above/below c_{crit} (Figures 3E–3G).

To rule out potential effects of droplet formation on global transcription activation, we examined global transcription signals and RNA Pol II localization above/below c_{crit} (Figures S3F–S3I). We found no global inhibition of transcription above c_{crit} for PHR-VPR or reinforced PHR-VP16 droplets as assayed by ethynyl-uridine (EU) staining (Figures S3F and S3G). Immunostaining showed no or very weak colocalization of RNA Pol II with VPR

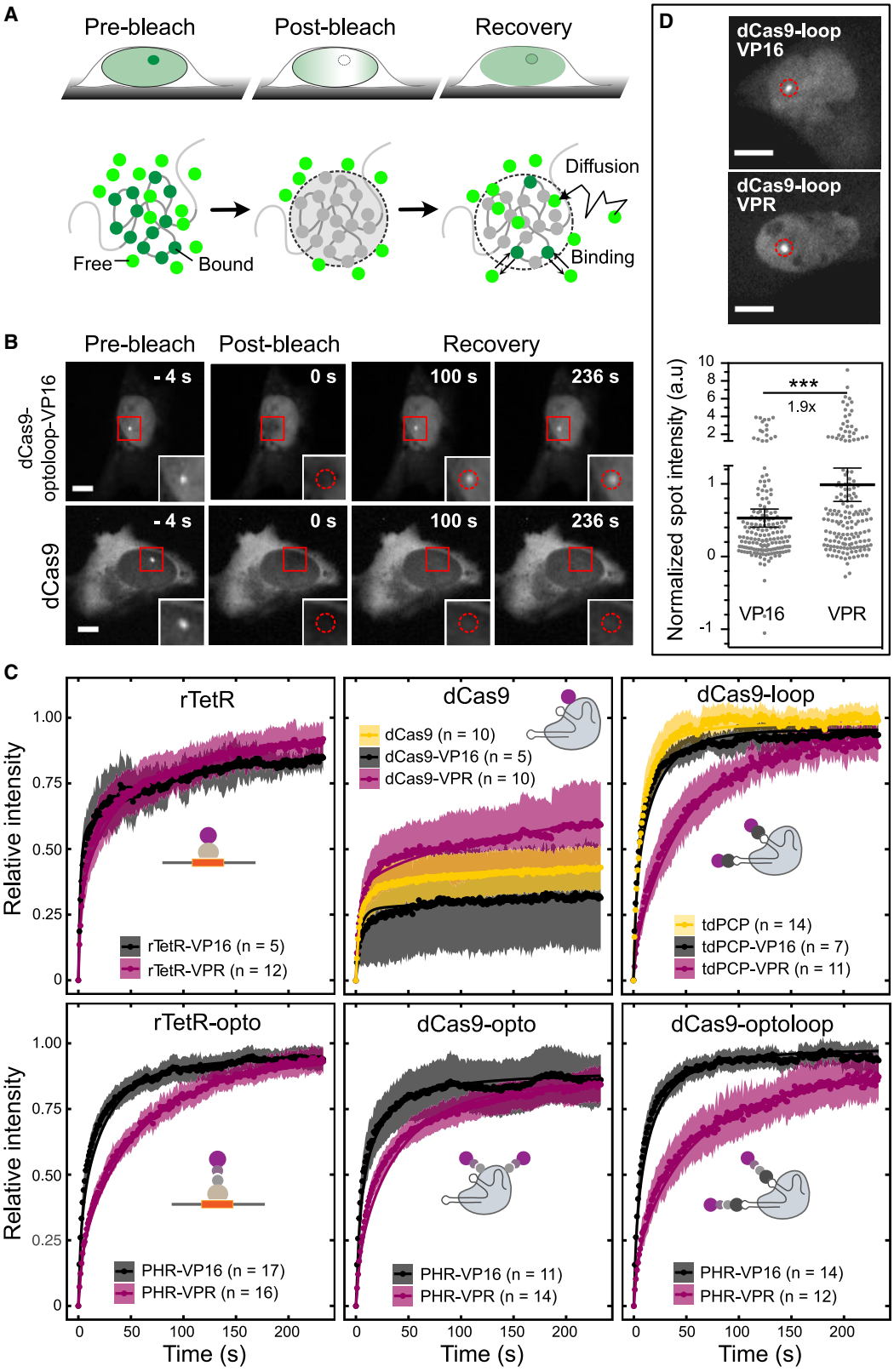

(legend on next page)

droplets (Figure S3H). The transcription initiation competent RNA Pol II S5P did not colocalize with droplets driven by bridging factors but was enriched in PHR-VPR droplets of some cells (Figure S3H). RNA Pol II and Pol II S5P were clearly enriched at the reporter array with bound PHR-VPR. RNA Pol II S5P punctae typically exceeded droplets in size and also were present in their absence (Figure S3H). This suggests nucleation of VPR droplets at pre-existing RNA Pol II S5P clusters as described previously (Wei et al., 2020), rather than droplet-driven sequestration of RNA Pol II S5P. Reinforced VP16 droplets showed no colocalization with RNA Pol II or Pol II S5P (Figure S3I). Thus, droplet formation did not globally inhibit transcription or limit the amount of RNA Pol II at the reporter array. We conclude that the additional enrichment of ADs in droplets above c_{crit} at and outside the reporter had no significant effect on transcriptional activation in our system. Moreover, certain types of droplets such as those containing bridging factors can inhibit transcription despite the accumulation of more AD molecules at the reporter array.

TF residence times are determined by both the DBD and the AD

Increased TF binding to chromatin is one parameter that could link multivalent interactions to stronger activation. In particular, the TF residence time could be affected by stabilizing multivalent interactions independent of an increased local enrichment of the TF by a phase separation process. To explore this model, we conducted a FRAP analysis of TF constructs containing an AD with either high (VPR) or low (VP16) propensity to engage in multivalent interactions (Figures 5 and S4). The recovery curves of TFs bound at the reporter array were fitted by a reaction-diffusion model for clustered binding sites (Sprague et al., 2006) (STAR Methods). This analysis yielded the apparent diffusion coefficient D_{eff}, the dissociation rate k_{off}, and the immobile fraction of stably bound molecules during the observation period of 240 s (Table S6). Residence times in the bound state ranged from τ_{res} < 10 s for tdPCP binding to PP7-loops to τ_{res} >240 s for DNA-bound dCas9-VP16 (Table S6; Figure 5C). Interestingly, the residence times for VPR compared with VP16 were consistently >24 s higher in the highly dynamic loop, opto, optoloop, and rTetR-opto complexes (Figure 5C). This delayed recovery points to VPR self-interactions that stabilize the binding of the tdPCP-VPR and PHR-VPR constructs. For the already very stably chromatin-bound dCas9-AD constructs, the VPR-VPR interactions manifested themselves as an additional faster exchanging contribution to the recovery that is visible for dCas9-VPR but absent in dCas9-VP16. To confirm the presence of additional proteins indirectly bound to the array, we measured the intensity of VPR and VP16 assemblies bound via the loop configuration (Figure 5D). We found a 1.9-fold higher signal for VPR compared with VP16 (p = 0.0006, Welch two-sample t test), confirming the additional recruitment seen in FRAP (Figure 5C, upper row third panel). We conclude that the TF residence time was not only dependent on the DBD but significantly influenced by the AD properties. VPR promoted the indirect binding of additional AD molecules to those that were already bound to DNA and stabilized the directly bound proteins in the case of weaker interactions. The enrichment of VPR via protein-protein interactions is likely to reflect multivalent interactions and is linked to its propensity to form droplets.

Transcription activation can occur independent of BRD4 and H3K27ac

TFs initiate transcription via different mechanisms that include the assembly of the transcription machinery, open complex formation, and establishing permissive chromatin states (Lionnet and Wu, 2021; Soto et al., 2022; Wong and Gunawardena, 2020). To unravel how these aspects are linked to the multivalent interaction and TF residence time, we correlated the activity of our TF constructs with the enrichment of BRD4 and H3K27ac—two prototypical marks of active transcription (Figure 6). TF activity was determined by qRT-PCR measurements of total reporter RNA levels (Figure 6A; Table S7) 24 h after induction. Moreover, nascent RNA, BRD4, and H3K27ac enrichment were measured by fluorescence microscopy (Figure 6B) to yield normalized radial profiles across the gene array (Figure 6C). The dCas9-opto and dCas9-optoloop constructs were clearly enriched but failed to activate the reporter (Figures 6A and S1A). This observation could be related to the heterochromatic state of the reporter (Janicki et al., 2004), in line with the variable efficiencies in transcriptional activation reported for similar constructs at endogenous promoters (Polstein and Gersbach, 2015) (Figures S5A–S5C). Nevertheless, dCas9-opto/optoloop efficiently induced BRD4 recruitment and H3K27 acetylation when coupled with VPR (Figures 6C, 6G, and 6H). All other TFs were able to activate transcription. VPR was a stronger activator than VP16 (Figure 6A) and displayed a much higher BRD4 and H3K27ac enrichment than VP16 did in most cases (Figure 6C). As a control, we recruited the histone acetyltransferase p300 core domain fused to dCas9 (Hilton et al., 2015; Shrimp et al., 2018), which resulted in H3K27ac and BRD4 accumulation but no RNA production. Notably, the inactive dCas9-opto and dCas9-optoloop complexes induced a similar enrichment pattern. We conclude that transcription activation can occur in parallel to these two marks of active transcription and distinguish

Figure 5. FRAP analysis of TF constructs with high- or low-phase separation propensity

(A) FRAP reaction-diffusion analysis of TF binding to reporter gene array. After bleaching of GFP-tagged constructs, fluorescence recovers by both diffusion of free molecules and exchange of bound molecules at the reporter gene array (dashed circle).

(B) Exemplary FRAP image series for the dCas9-optoloop-VP16 complex (top) with fast exchange and for dCas9 alone (bottom) with no exchange during the observation period. Scale bar, 10 μm.

(C) Averaged FRAP curves and 95% CI of VP16 and VPR constructs with the indicated DNA-binding modules. Constructs were recruited to *lac*O except for the *tet*O-dependent constructs. Solid lines represent the fit to a reaction-diffusion model for clustered binding sites.

(D) Reporter array enrichment of VP16 and VPR recruited via dCas9-loop. GFP signal was background subtracted and normalized to the tagBFP-LacI marker. The 1.9-fold higher signal for VPR indicates additional molecules bound indirectly to chromatin. Solid bar, mean; error bar, 95% CI; n = 164–166 cells per condition; ***p < 0.001, unpaired two-sided Welch's t test. Scale bar, 10 μm.

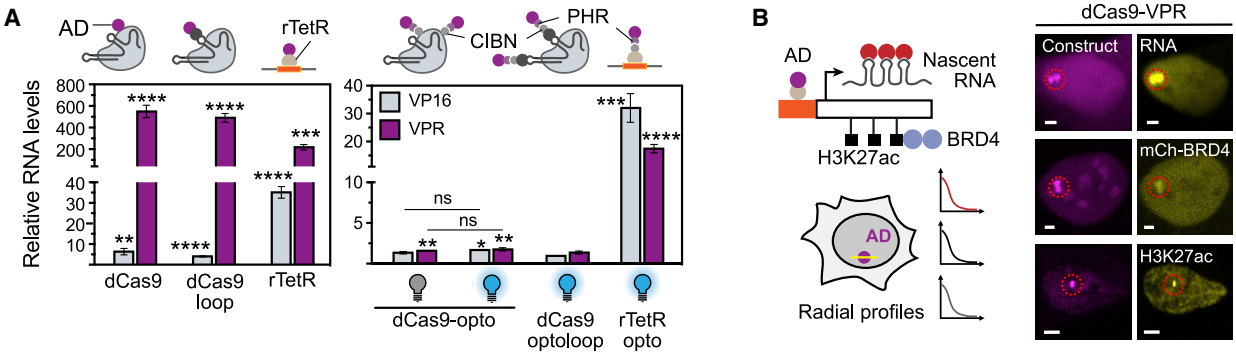

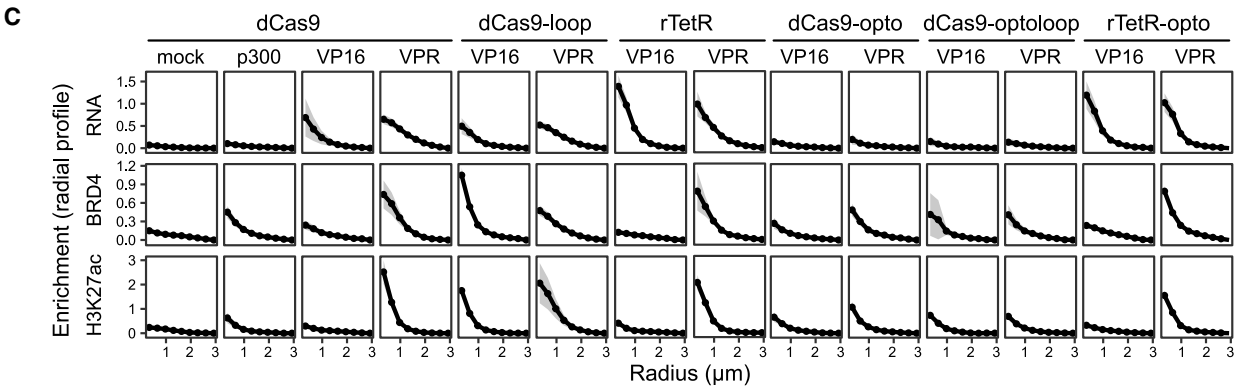

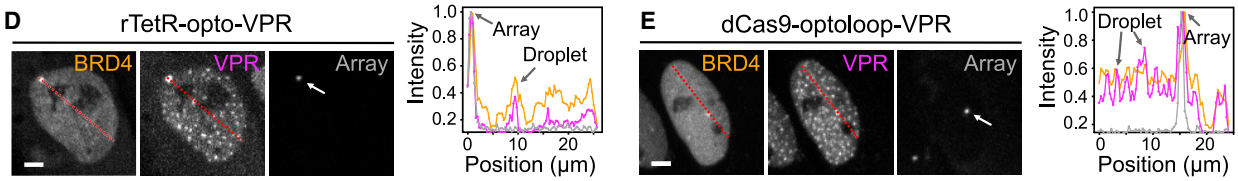

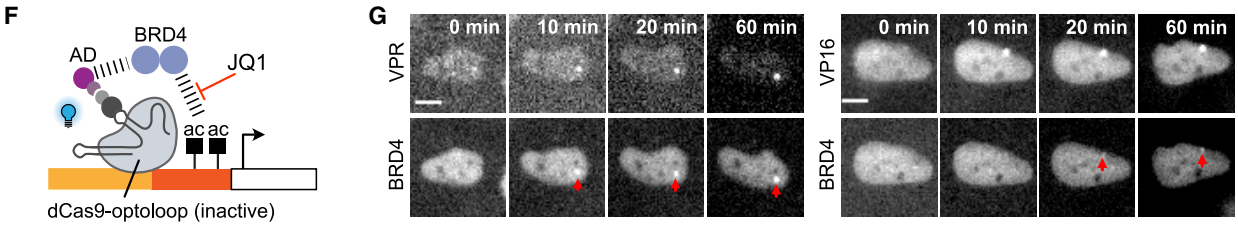

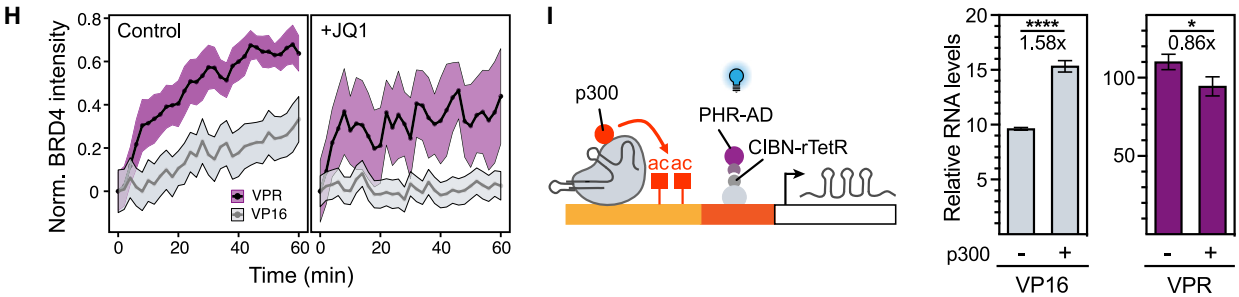

(legend on next page)

three TF types: (1) strong activators such as dCas9-VPR and rTetR-VPR that induce both transcription and strong enrichment of BRD4 and H3K27ac, (2) activators represented by rTetR-VP16 that displayed moderate but robust activation at very low levels of BRD4 and H3K27ac, and (3) the dCas9-opto/optoloop constructs that efficiently recruited BRD4 and induced acetylation but failed to activate transcription.

VPR recruits BRD4 directly and is less dependent on pre-existing histone acetylation

We observed that both activating and nonactivating opto complexes with VPR enriched over-expressed mCherry-BRD4 in optodroplets, while this was hardly observed for VP16 (Figures 6D and 6E). Thus, we hypothesized that transient multivalent interactions between VPR and BRD4 could contribute to the faster (Figure 3B) and stronger (Figure 6A) activation. To test this, we used the inactive dCas9-optoloop complex as a tool to monitor VP16 or VPR-dependent BRD4 accumulation in the absence of transcription (Figures 6F and 6G). VPR induced a faster accumulation of BRD4 to higher levels than VP16 (Figure 6H). An initial steep rise of BRD4 recruitment over the first 10 min was apparent for VPR but absent for VP16, which was followed by a phase of slower BRD4 accumulation. Next, we treated the cells with the inhibitor JQ1 that disrupts BRD4 bromodomain interactions with acetylated histones (Figure 6H). JQ1 pretreatment completely abrogated BRD4 accumulation for VP16. For VPR, the initial steep rise remained unaffected, but BRD4 binding in the second phase was reduced. These kinetics suggest a direct VPR-BRD4 interaction within the first phase, whereas the subsequent BRD4 accumulation could reflect binding to newly acetylated histones via its bromodomain, which would be inhibited by JQ1. We repeated the JQ1 treatment with the transcriptionally active rTetR-opto-VP16 and -VPR constructs to study the impact of BRD4 on transcriptional activation. JQ1 did not reduce nascent RNA production by VP16 or VPR (Figure S5D; Table S8), whereas total reporter RNA levels were reduced for VPR (1.8-fold reduction) but mostly unaffected for VP16 (1.1-fold reduction) (Figure S5E; Table S7). We conclude that BRD4 accumulation accompanies transcriptional activation but is not essential. It may, however, enhance activation by VPR or stabilize activated states.

To test whether histone acetylation contributes to the strong activation capacity of VPR, we constitutively recruited dCas9-p300core to the distal *lac*O sites of the reporter (Figure 6I; Table S7). This allowed us to compare transcriptional induction by rTetR-opto VP16 and VPR in the presence or absence of pre-established (p300-dependent) histone acetylation. VP16 produced higher total levels of reporter RNA in the presence of dCas9-p300 compared with the control (dCas9-GFP), whereas VPR did not. Nascent RNA time courses revealed a stronger increase in the plateau level for VP16 (3.1-fold) than for VPR (2.1-fold) (Figures S5F and S5G; Table S8). We conclude that pre-existing histone acetylation can increase the transcription induction more strongly for VP16 than for VPR. Even though the two activators differ in their strength, the lower activity of VP16 could be related in part to a reduced ability to bind histone acetylases such as p300 as well as BRD4.

Shortened residence times reduce activation capacity independent of binding site occupancy

Our results support a model in which multivalent AD interactions enhance the transcriptional activation capacity of a TF by increasing its residence time in the promoter-bound state and by recruiting cofactors. To test whether changes in residence time indeed affect the activation capacity independent of binding site occupancy, we artificially increased the turnover of reporter-bound dCas9-VP16 or VPR constructs by introducing a single nucleotide mutation into the sgRNA targeting the *tet*O repeats of the reporter (sgRNA-mut) (Figures 7A and S6A; Table S3). FRAP analysis for the dCas9-VPR construct confirmed a decrease in residence time from sgRNA-wt (wild type): τ_{res} = 83 s (95% confidence interval (CI): 47–342 s) to sgRNA-mut (mutated): τ_{res} = 48 s (95% CI: 32–94 s) (Figure 7B; Table S6). Furthermore, the immobile fraction was lowered from 34% to 7% (95% CIs: 22%–47% and 0%–16%). Next, we compared transcription activation between the fast and slowly exchanging complexes. For fast exchanging complexes, occupancy was reduced by 2.7 (VPR) and 7.2-fold (VP16), respectively

Figure 6. Transcription activation features in dependence of TF architecture and AD type

(A) qRT-PCR quantification of total reporter RNA levels for different TF constructs 24 h post-induction. rTetR and opto(loop) constructs were activated by the addition of doxycycline and/or constant illumination. Mean and SD of fold-change induction compared with mock-transfected samples and normalized to β-actin mRNA (n = 3). Two-sided unpaired Student's t test compared with the mock condition, not significant (ns), *p < 0.05, **p < 0.01, ***p < 0.001, ****p < 0.0001.

(B) Scheme and representative images for radial enrichment analysis of steady-state nascent RNA levels (tdMCP), cofactor binding (mCherry-BRD4), and activation marks (H3K27ac) at the reporter (dashed circle), 24h post-induction. Scale bar, 5 μm.

(C) Radial enrichment profiles of RNA, BRD4, and H3K27ac for all TF constructs with either VP16 or VPR as AD (average of n = 16–520 cells per condition). dCas9 alone (mock) and dCas9-p300core were included as controls.

(D) Colocalization of mCherry-BRD4 with PHR-VPR droplets upon recruitment via rTetR-opto. Intensity profiles (dashed lines) showing the enrichment of BRD4 (orange) in some of the droplets (pink) and at the reporter (gray, LacI marker). Intensities were normalized to the maximum value within each channel. Scale bar, 5 μm.

(E) Same as (D), but for the dCas9-optoloop-VPR construct.

(F) Experimental setup to compare VP16 and VPR-dependent BRD4 recruitment in the absence of transcription using the inactive dCas9-optoloop complex bound to both *tet*O and *lac*O sites. Pretreatment with JQ1 distinguishes direct from acetylation-dependent BRD4 binding.

(G) Representative time courses of BRD4 enrichment at the reporter (arrows) for VPR and VP16 without JQ1. Scale bar, 10 μm.

(H) Time traces of BRD4 signal accumulation at the reporter after light-induced VPR/VP16 binding with or without JQ1 (1 μM, 3 h pre-induction). Mean values of normalized intensity and 95% CI are shown for n = 10–85 cells per condition.

(I) Transcriptional activation by rTetR-opto-VP16 and -VPR in dependence of histone acetylation pre-established by dCas9-p300core bound to the *lac*O sites of the reporter. Total reporter RNA after 90-min activation was measured by qRT-PCR and is shown as fold changes for dCas9-p300 (+) relative to dCas9 alone (−). Mean and SD of reporter RNA levels (n = 3) normalized to β-actin mRNA. Two-sided unpaired Student's t test, *p < 0.05 and ****p < 0.0001.

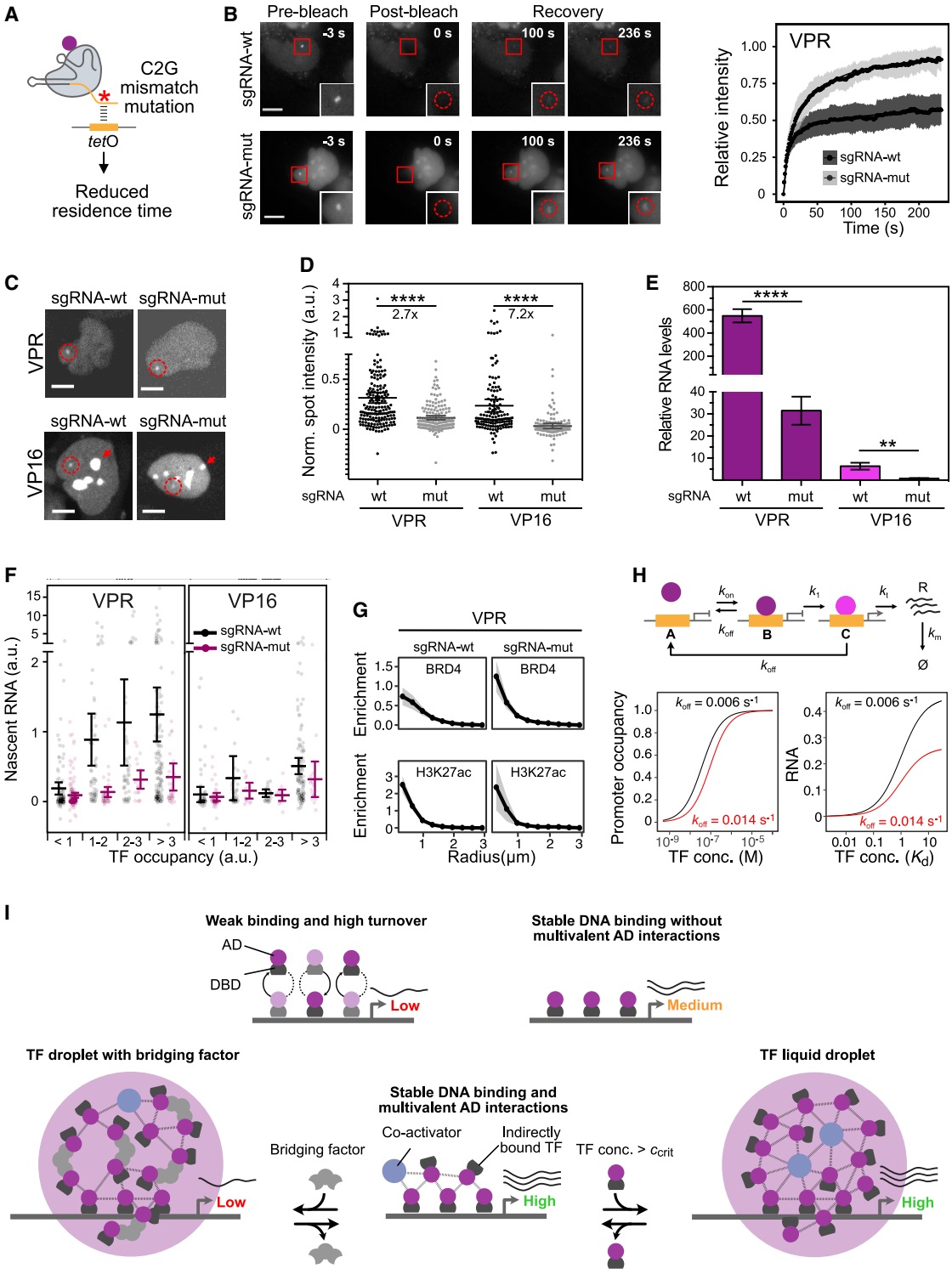

Figure 7. Transcription activation in dependence of TF residence time, binding site occupancy, and multivalent interactions

(A) A C2G mismatch mutation in the targeting sgRNA (sgRNA-mut) was used to reduce dCas9 residence time.

(B) FRAP image series (left), averaged recovery curves with 95% CI (right) of dCas9-VPR recruited via sgRNA-wt (n = 10) or sgRNA-mut (n = 7).

(C) Representative images showing enrichment of dCas9-VP16/-VPR at the reporter (dashed circle, position determined by cotransfected LacI marker) for both conditions. The VP16 construct was also enriched in nucleoli (arrows).

(legend continued on next page)

(Figures 7C and 7D). The fraction of cells with visible dCas9 recruitment decreased from 90% to 76% (VPR) and from 59% to 17% (VP16) (Figure S6B; Table S9). Total reporter RNA levels were strongly reduced for both VP16 and VPR (Figure 7E). An increase of occupancy with activator concentration was observed, which is likely due to indirectly recruited molecules via multivalent interactions (Figure S6C). As expected, RNA production increased with occupancy. To separate the effect of occupancy and residence time, we binned cells into groups with equal occupancy and compared their nascent RNA production (Figure 7F). The average RNA production by VPR was consistently lower for the fast (sgRNA-mut) versus the slowly (sgRNA-wt) exchanging complex within each occupancy group (VPR: 2- to 6-fold, VP16: 1.3- to 2-fold; VPR: $p < 0.001$, VP16: $p > 0.05$, two-way ANOVA of occupancy group and sgRNA). We also measured the radial BRD4 and H3K27ac enrichment profiles and observed a robust enrichment even with reduced VPR residence times (Figure 7G). This corroborates our previous findings that BRD4 recruitment and histone acetylation occur efficiently even at a high AD turnover rate. The residence time dependency of activation shown in Figure 7F suggests that the TF is involved in an energy-dependent activation step. A kinetic model demonstrated that the measured ~2-fold difference in residence time can become a key determinant of transcription output independent of binding site occupancy (Figure 7H, STAR Methods). Furthermore, the higher sensitivity of VP16-mediated activation to a reduction of its residence time suggests that multivalent interactions of VPR can at least partly compensate for reduced DNA binding.

DISCUSSION

By comparing a panel of TF constructs, we dissected contributions from the DBD, multivalent AD interactions, phase separation, coactivator recruitment, and histone acetylation to transcription activation. The main results and conclusions are summarized in Figure 7I. The ADs studied here fell into two classes based on their propensity to form optodroplets (Figures 1C, 1D, and 3): ADs with a high potential to engage in multivalent interactions and a strong activation capacity (p65, Rta, and VPR) versus those with weaker multivalent interactions and lower activation capacity (STAT2 and VP16). Higher multivalency stabilized chromatin binding and led to the accumulation of additional molecules via protein-protein interactions (Figure 5). Likewise, the coactivator network centered around BRD4, p300, and H3K27ac was more strongly associated with VPR than with VP16 (Figures 6B–6I). This is in line with previous reports on the ability of BRD4 and p300 to engage in dynamic multivalent interactions (Cho et al., 2018; Han et al., 2020; Ma et al., 2021; Sabari et al., 2018; Zhang et al., 2021). It is noted that BRD4 was neither required nor sufficient to induce transcription in our experiments (Figures 6C, S5D, and S5E) and transcription was not a prerequisite for BRD4 binding or H3K27 acetylation (Figure 6C).

We show that TF activation strength is reduced with shorter residence times independent of TF-binding site occupancy (Figure 7F). This finding corroborates conclusions from previous studies (Callegari et al., 2019; Gurdon et al., 2020; Loffreda et al., 2017; Popp et al., 2021; Shelansky and Boeger, 2020). It indicates that TF binding is coupled to an energy-dependent kinetic proofreading step similar to nucleosome remodeling, promoter DNA melting, or post-translational modifications of chromatin or TFs as illustrated in the model depicted in Figure 7H (Loffreda et al., 2017; Shelansky and Boeger, 2020; Wong and Gunawardena, 2020; Yang et al., 2010). Interestingly, BRD4 enrichment around the promoter could also be maintained with weakened DNA binding and high turnover in the mutated sgRNA experiments, suggesting that it is not critically dependent on the residence time (Figure 7G).

LLPS of PHR/CRY2 constructs with TAF15 (Wei et al., 2020) or VP16 fused to IDRs like FUSN (Schneider et al., 2021) have been reported to amplify gene expression and to increase transcription activation. Furthermore, it has been proposed that condensates at super-enhancers drive the transcription of highly active genes (Hnisz et al., 2017; Sabari et al., 2018; Shrinivas et al., 2019). These previous studies attributed activation to a local TF enrichment by LLPS based on the comparison to control constructs without IDRs and/or in the absence of a light trigger. However, experiments that assess transcription activity of the same chromatin-bound activator in the presence/absence of droplet formation under identical conditions were lacking. Our optogenetic AD constructs allowed us to compare identical TF constructs above and below c_{crit}.

(D) Enrichment of dCas9-VP16/-VPR with wildtype and mutated sgRNA (n = 127–175 cells per condition, Table S9). Intensities were background subtracted and normalized to LacI marker intensity. Solid bar, mean; error bars, 95% CI; ****$p < 0.0001$, two-sided Welch's t test.

(E) Total reporter RNA levels 24h post-transfection for sgRNA-wt/mut. Mean and SD of fold-change versus mock-transfected samples and normalized to β-actin mRNA (n = 3). Two-sided unpaired Student's t test, **$p < 0.01$, ****$p < 0.0001$. The data for sgRNA-wt are the same as in Figure 6A.

(F) Steady-state nascent RNA levels of single cells 24h post-transfection, divided into groups with equal TF occupancies determined from the AD signal normalized to the LacI marker. Mean and 95% CI are indicated. Note the axis break for improved visualization.

(G) Radial enrichment profiles for mCherry-BRD4 and H3K27ac for high and low residence time of dCas9-VPR. Data for sgRNA-wt are the same as in Figure 6C. Mean and 95 % CI; n = 28–184 cells per condition.

(H) Multistep transcription activation mechanism with RNA production limited by TF residence time (STAR Methods). After TF binding (state B), another energy-dependent transition to state C is required to produce RNA with rate k_1. Two different dissociation rates $k_{off} = 0.006\ s^{-1}$ ($\tau_{res} = 167$ s) and $k_{off} = 0.014\ s^{-1}$ ($\tau_{res} = 71$ s) as observed in FRAP experiments were compared. Binding site occupancy (bottom, left) was computed for $k_{on} = 10^5\ M^{-1}\ s^{-1}$, corresponding to a K_d of 60 and 140 nM, respectively. Steady-state RNA levels (bottom, right) are shown as a function of TF concentration in K_d units, that is, for the same promoter occupancy.

(I) Summary of the dependence of transcription on TF residence time, multivalent interactions, and phase separation. Low residence times lead to lower transcription. Multivalent AD interactions increase transcription activation capacity by stabilization of binding and in part via cofactor interactions. The capability of the AD to establish multivalent interactions manifests itself in its propensity to form phase-separated droplets. In our system, LLPS increased the local TF concentration but did not further enhance transcription. TF droplets induced by bridging factors can inhibit transcription despite a strong TF enrichment at the promoter.

We found that the presence or absence of ectopic optodroplets reliably stratified cells into two groups with biophysically distinct states of AD accumulations at the reporter (Figure 2). Above c_{crit}, ADs with high multivalency accumulated into subdomains with liquid-like properties that remained separated. Importantly, TFs did not form a single spherical and homogeneous compartment at the reporter as would be expected from *in vitro* studies with solutions of purified protein and DNA (Boija et al., 2018). Instead, our results are compatible with the model of isolated TF microdroplets that assemble at the chromatin-binding site scaffold provided by the reporter array in a surface condensation process, conceptionally similar to the recently described formation of TF foci on λ-DNA *in vitro* (Morin et al., 2022). However, it is noted that in our system, the localized AD accumulation at the reporter array occurred above c_{crit} as defined by the concentration threshold for the formation of ectopic droplets.

When comparing cells above and below c_{crit}, we saw no significant effect of droplet formation on transcription activation by p65, Rta, VPR, and FUSN-VP16 (Figures 3E–3G, 4C, and 4K). Reinforcing TF droplet formation via the addition of bridging factors had an inhibitory effect (Figure 4). Interestingly, a recent report found that an oncogenic fusion TF shows its highest activity only inside a certain range of multivalent interactions (Chong et al., 2022). Furthermore, transcription suppression has been observed by sequestration of RNA polymerase I into a phase-separated subcompartment at the nucleolar cap (Ide et al., 2020). Whether inhibitory TF phase separation is involved in regulating RNA Pol II activity in an endogenous cellular environment, for example, to establish refractory promoter states, remains to be demonstrated.

We argue that multivalent AD interactions that frequently involve IDRs are sufficient to enhance transcription below c_{crit} for droplet formation. LLPS of TFs above c_{crit} might therefore reflect intrinsic AD properties to mediate interactions with coactivators but without occurring under endogenous conditions as discussed previously (Chong et al., 2018; Rippe, 2022; Rippe and Papantonis, 2022). In this scenario, direct DNA binding of a TF via its DBD is stabilized by protein-protein interactions of ADs such as VPR that mediate the indirect binding of additional TFs and cofactors (Figure 7I). The resulting acetylation of histones or the TF itself (Loffreda et al., 2017; Yang et al., 2010) could further stabilize the chromatin-bound state. While indirectly bound factors exchange fast, the two-layered complex of directly and indirectly bound TFs and coactivators would still be defined by stoichiometric binding of its components. Thus, it is important to distinguish its activity from the effect of further nonstoichiometric accumulation of factors into liquid droplets to assess the potential contribution of LLPS to transcription activation.

Limitations of the study

Our conclusions on the functional relevance of phase-separated TF assemblies are based on optogenetic constructs recruited to a reporter gene array. We did not address the question whether a corresponding LLPS process would occur for endogenous TFs at an endogenous gene cluster. Thus, it remains to be investigated to which extent the findings and conclusions obtained here apply to transcription in other systems. Furthermore, our characterization of AD assembly above/below c_{crit} is limited by the resolution of the microscopy methods applied. We cannot rule out that small "nanodroplets" assemble already below c_{crit} at the array and remain undetected at the resolution of our dSTORM analysis. Finally, modulating dCas9 binding by introducing a single sgRNA mutation allowed us to compare largely different residence times between two otherwise identical activators. It is noted that the residence time of dCas9 is one or two orders of magnitude higher than values typically observed for endogenous TFs, although molecular subpopulations with comparably long residence times can exist (Garcia et al., 2021; Gurdon et al., 2020; Lu and Lionnet, 2021). Accordingly, the functionally relevant timescales of endogenous TFs in their chromatin-bound state need to be further dissected to corroborate the conclusion that the TF residence time can be rate limiting for the transcription activation process.

STAR★METHODS

Detailed methods are provided in the online version of this paper and include the following:

- KEY RESOURCES TABLE
- RESOURCE AVAILABILITY
  - Lead contact
  - Materials availability
  - Data and code availability
- EXPERIMENTAL MODEL AND SUBJECT DETAILS
  - Cell lines
- METHOD DETAILS
  - Plasmids
  - Cell culture
  - RNA isolation and qRT-PCR
  - Microscopy instrumentation
  - High resolution imaging (SRRF and dSTORM)
  - Droplet fusion videos and half-spot FRAP
  - Light-induced time course experiments
  - Analysis of time course images
  - Light-induced optodroplet formation
  - FRAP analysis
  - Comparison of FRAP for widefield and confocal microscopy setup
  - Quantification of images for FRAP analysis
  - Theoretical framework for FRAP analysis of clustered binding sites
  - Parameter estimation from recovery curves
  - Model for TF residence time dependent activation
  - Analysis of binding and dissociation kinetics
  - Immunofluorescence
  - Ethynyl-uridine staining
  - Single molecule RNA FISH
  - Radial profiles, spot intensities and areas
  - Image analysis software
- QUANTIFICATION AND STATISTICAL ANALYSIS

SUPPLEMENTAL INFORMATION

Supplemental information can be found online at https://doi.org/10.1016/j.molcel.2022.04.017.

ACKNOWLEDGMENTS

We thank Robin Weinmann and Fabian Erdel for discussions and the Bioquant advanced biological screening facility and the DKFZ light microscopy core facility for help. This project was supported by grant RI1283/16-1 in the Priority Program 2191 "Molecular Mechanisms of Functional Phase Separation" of the Deutsche Forschungsgemeinschaft (DFG) and the START-HD Explorer project of the University of Heidelberg. Data storage at SDS@hd was funded by the Ministry of Science, Research, and the Arts Baden-Württemberg (MWK) and the DFG through grants INST 35/1314-1 FUGG and INST 35/1503-1 FUGG.

AUTHOR CONTRIBUTIONS

Study design, K.R., J.T., and L.F.; acquisition of data, J.T., L.F., A.R., N.M., and P.G.; analysis of data, J.T., L.F., A.R., N.M., and K.R.; drafting of manuscript, J.T., L.F., and K.R.; manuscript reviewing: all authors; supervision and coordination, K.R.

DECLARATION OF INTERESTS

The authors declare no competing interests.

Received: July 14, 2021
Revised: February 28, 2022
Accepted: April 11, 2022
Published: May 9, 2022

SUPPORTING CITATIONS

Frahm et al., 2006, Frank et al., 2021, Günther et al., 2013, Jegou et al., 2009, Rafalska-Metcalf et al., 2010, Rothbauer et al., 2008.

REFERENCES

Banani, S.F., Lee, H.O., Hyman, A.A., and Rosen, M.K. (2017). Biomolecular condensates: Organizers of cellular biochemistry. Nat. Rev. Mol. Cell Biol. *18*, 285–298.

Boija, A., Klein, I.A., Sabari, B.R., Dall'Agnese, A., Coffey, E.L., Zamudio, A.V., Li, C.H., Shrinivas, K., Manteiga, J.C., Hannett, N.M., et al. (2018). Transcription factors activate genes through the phase-separation capacity of their activation domains. Cell *175*, 1842–1855.e16.

Bracha, D., Walls, M.T., Wei, M.T., Zhu, L., Kurian, M., Avalos, J.L., Toettcher, J.E., and Brangwynne, C.P. (2018). Mapping local and global liquid phase behavior in living cells using photo-oligomerizable seeds. Cell *175*, 1467–1480.e13.

Brent, R., and Ptashne, M. (1985). A eukaryotic transcriptional activator bearing the DNA specificity of a prokaryotic repressor. Cell *43*, 729–736.

Callegari, A., Sieben, C., Benke, A., Suter, D.M., Fierz, B., Mazza, D., and Manley, S. (2019). Single-molecule dynamics and genome-wide transcriptomics reveal that NF-kB (p65)-DNA binding times can be decoupled from transcriptional activation. PLoS Genet *15*, e1007891.

Chavez, A., Scheiman, J., Vora, S., Pruitt, B.W., Tuttle, M., P R Iyer, E., Lin, S., Kiani, S., Guzman, C.D., Wiegand, D.J., et al. (2015). Highly efficient Cas9-mediated transcriptional programming. Nat. Methods *12*, 326–328.

Cho, W.K., Spille, J.H., Hecht, M., Lee, C., Li, C., Grube, V., and Cisse, I.I. (2018). Mediator and RNA polymerase II clusters associate in transcription-dependent condensates. Science *361*, 412–415.

Choi, J.M., Holehouse, A.S., and Pappu, R.V. (2020). Physical principles underlying the complex biology of intracellular phase transitions. Annu. Rev. Biophys. *49*, 107–133.

Chong, S., Dugast-Darzacq, C., Liu, Z., Dong, P., Dailey, G.M., Cattoglio, C., Heckert, A., Banala, S., Lavis, L., Darzacq, X., et al. (2018). Imaging dynamic and selective low-complexity domain interactions that control gene transcription. Science *361*, eaar2555.

Chong, S., Graham, T.G.W., Dugast-Darzacq, C., Dailey, G.M., Darzacq, X., and Tjian, R. (2022). Tuning levels of low-complexity domain interactions to modulate endogenous oncogenic transcription. Mol. Cell. *82*. https://doi.org/10.1016/j.molcel.2022.04.007.

Erdel, F., Rademacher, A., Vlijm, R., Tünnermann, J., Frank, L., Weinmann, R., Schweigert, E., Yserentant, K., Hummert, J., Bauer, C., et al. (2020). Mouse heterochromatin adopts digital compaction states without showing hallmarks of HP1-driven liquid-liquid phase separation. Mol. Cell *78*, 236–249.e7.

Erdel, F., and Rippe, K. (2018). Formation of chromatin subcompartments by phase separation. Biophys. J. *114*, 2262–2270.

Frahm, T., Hauser, H., and Köster, M. (2006). IFN-type-I-mediated signaling is regulated by modulation of STAT2 nuclear export. J. Cell Sci. *119*, 1092–1104.

Frank, L., Weinmann, R., Erdel, F., Trojanowski, J., and Rippe, K. (2021). Transcriptional activation of heterochromatin by recruitment of dCas9 activators. Methods Mol. Biol. *2351*, 307–320.

Garcia, D.A., Fettweis, G., Presman, D.M., Paakinaho, V., Jarzynski, C., Upadhyaya, A., and Hager, G.L. (2021). Power-law behavior of transcription factor dynamics at the single-molecule level implies a continuum affinity model. Nucleic Acids Res. *49*, 6605–6620.

Günther, K., Rust, M., Leers, J., Boettger, T., Scharfe, M., Jarek, M., Bartkuhn, M., and Renkawitz, R. (2013). Differential roles for MBD2 and MBD3 at methylated CpG islands, active promoters and binding to exon sequences. Nucleic Acids Res. *41*, 3010–3021.

Gurdon, J.B., Javed, K., Vodnala, M., and Garrett, N. (2020). Long-term association of a transcription factor with its chromatin binding site can stabilize gene expression and cell fate commitment. Proc. Natl. Acad. Sci. USA *117*, 15075–15084.

Gustafsson, N., Culley, S., Ashdown, G., Owen, D.M., Pereira, P.M., and Henriques, R. (2016). Fast live-cell conventional fluorophore nanoscopy with ImageJ through super-resolution radial fluctuations. Nat. Commun. *7*, 12471.

Han, X., Yu, D., Gu, R., Jia, Y., Wang, Q., Jaganathan, A., Yang, X., Yu, M., Babault, N., Zhao, C., et al. (2020). Roles of the BRD4 short isoform in phase separation and active gene transcription. Nat. Struct. Mol. Biol. *27*, 333–341.

Heilemann, M., van de Linde, S., Schüttpelz, M., Kasper, R., Seefeldt, B., Mukherjee, A., Tinnefeld, P., and Sauer, M. (2008). Subdiffraction-resolution fluorescence imaging with conventional fluorescent probes. Angew. Chem. Int. Ed. Engl. *47*, 6172–6176.

Hilton, I.B., D'Ippolito, A.M., Vockley, C.M., Thakore, P.I., Crawford, G.E., Reddy, T.E., and Gersbach, C.A. (2015). Epigenome editing by a CRISPR-Cas9-based acetyltransferase activates genes from promoters and enhancers. Nat. Biotechnol. *33*, 510–517.

Hnisz, D., Shrinivas, K., Young, R.A., Chakraborty, A.K., and Sharp, P.A. (2017). A phase separation model for transcriptional control. Cell *169*, 13–23.

Hopfield, J.J. (1974). Kinetic proofreading: a new mechanism for reducing errors in biosynthetic processes requiring high specificity. Proc. Natl. Acad. Sci. USA *71*, 4135–4139.

Ide, S., Imai, R., Ochi, H., and Maeshima, K. (2020). Transcriptional suppression of ribosomal DNA with phase separation. Sci. Adv. *6*. eabb5953.

Janicki, S.M., Tsukamoto, T., Salghetti, S.E., Tansey, W.P., Sachidanandam, R., Prasanth, K.V., Ried, T., Shav-Tal, Y., Bertrand, E., Singer, R.H., et al. (2004). From silencing to gene expression: Real-time analysis in single cells. Cell *116*, 683–698.

Jegou, T., Chung, I., Heuvelman, G., Wachsmuth, M., Görisch, S.M., Greulich-Bode, K.M., Boukamp, P., Lichter, P., and Rippe, K. (2009). Dynamics of telomeres and promyelocytic leukemia nuclear bodies in a telomerase-negative human cell line. Mol. Biol. Cell *20*, 2070–2082.

Kennedy, M.J., Hughes, R.M., Peteya, L.A., Schwartz, J.W., Ehlers, M.D., and Tucker, C.L. (2010). Rapid blue-light-mediated induction of protein interactions in living cells. Nat. Methods *7*, 973–975.

Kurosu, T., and Peterlin, B.M. (2004). VP16 and ubiquitin; binding of P-TEFb via its activation domain and ubiquitin facilitates elongation of transcription of target genes. Curr. Biol. *14*, 1112–1116.

Lewis, M., Chang, G., Horton, N.C., Kercher, M.A., Pace, H.C., Schumacher, M.A., Brennan, R.G., and Lu, P. (1996). Crystal structure of the lactose operon repressor and its complexes with DNA and inducer. Science *271*, 1247–1254.

Lionnet, T., and Wu, C. (2021). Single-molecule tracking of transcription protein dynamics in living cells: seeing is believing, but what are we seeing? Curr. Opin. Genet. Dev. *67*, 94–102.

Loffreda, A., Jacchetti, E., Antunes, S., Rainone, P., Daniele, T., Morisaki, T., Bianchi, M.E., Tacchetti, C., and Mazza, D. (2017). Live-cell p53 single-molecule binding is modulated by C-terminal acetylation and correlates with transcriptional activity. Nat. Commun. *8*, 313.

Lu, F., and Lionnet, T. (2021). Transcription factor dynamics. Cold Spring Harb. Perspect. Biol. *13*, a040949.

Ma, L., Gao, Z., Wu, J., Zhong, B., Xie, Y., Huang, W., and Lin, Y. (2021). Co-condensation between transcription factor and coactivator p300 modulates transcriptional bursting kinetics. Mol. Cell *81*, 1682–1697.e7.

Mazzocca, M., Fillot, T., Loffreda, A., Gnani, D., and Mazza, D. (2021). The needle and the haystack: Single molecule tracking to probe the transcription factor search in eukaryotes. Biochem. Soc. Trans. *49*, 1121–1132.

McSwiggen, D.T., Mir, M., Darzacq, X., and Tjian, R. (2019). Evaluating phase separation in live cells: diagnosis, caveats, and functional consequences. Genes Dev *33*, 1619–1634.

Morin, J.A., Wittmann, S., Choubey, S., Klosin, A., Golfier, S., Hyman, A.A., Jülicher, F., and Grill, S.W. (2022). Sequence-dependent surface condensation of a pioneer transcription factor on DNA. Nat. Phys. *18*, 271–276.

Müller-Ott, K., Erdel, F., Matveeva, A., Mallm, J.P., Rademacher, A., Hahn, M., Bauer, C., Zhang, Q., Kaltofen, S., Schotta, G., et al. (2014). Specificity, propagation, and memory of pericentric heterochromatin. Mol. Syst. Biol. *10*, 746.

Ovesný, M., Křížek, P., Borkovec, J., Svindrych, Z., and Hagen, G.M. (2014). ThunderSTORM: A comprehensive ImageJ plug-in for PALM and STORM data analysis and super-resolution imaging. Bioinformatics *30*, 2389–2390.

Pankert, T., Jegou, T., Caudron-Herger, M., and Rippe, K. (2017). Tethering RNA to chromatin for fluorescence microscopy based analysis of nuclear organization. Methods *123*, 89–101.

Patel, A., Lee, H.O., Jawerth, L., Maharana, S., Jahnel, M., Hein, M.Y., Stoynov, S., Mahamid, J., Saha, S., Franzmann, T.M., et al. (2015). A liquid-to-solid phase transition of the ALS protein FUS accelerated by disease mutation. Cell *162*, 1066–1077.

Pau, G., Fuchs, F., Sklyar, O., Boutros, M., and Huber, W. (2010). EBImage – an R package for image processing with applications to cellular phenotypes. Bioinformatics *26*, 979–981.

Polstein, L.R., and Gersbach, C.A. (2015). A light-inducible CRISPR-Cas9 system for control of endogenous gene activation. Nat. Chem. Biol. *11*, 198–200.

Popp, A.P., Hettich, J., and Gebhardt, J.C.M. (2021). Altering transcription factor binding reveals comprehensive transcriptional kinetics of a basic gene. Nucleic Acids Res. *49*, 6249–6266.

R Core Team (2020). R: A language and environment for statistical computing (R Foundation for Statistical Computing). Austria URL. https://www.R-project.org/.

Rademacher, A., Erdel, F., Trojanowski, J., Schumacher, S., and Rippe, K. (2017). Real-time observation of light-controlled transcription in living cells. J. Cell Sci. *130*, 4213–4224.

Rafalska-Metcalf, I.U., Powers, S.L., Joo, L.M., LeRoy, G., and Janicki, S.M. (2010). Single cell analysis of transcriptional activation dynamics. PLoS One *5*, e10272.

Rippe, K. (2022). Liquid-liquid phase separation in chromatin. Cold Spring Harb. Perspect. Biol. *14*, a040683.

Rippe, K., and Papantonis, A. (2022). Functional organization of RNA polymerase II in nuclear subcompartments. Curr. Opin. Cell Biol. *74*, 88–96.

Rothbauer, U., Zolghadr, K., Muyldermans, S., Schepers, A., Cardoso, M.C., and Leonhardt, H. (2008). A versatile nanotrap for biochemical and functional studies with fluorescent fusion proteins. Mol. Cell. Proteomics *7*, 282–289.

Sabari, B.R. (2020). Biomolecular condensates and gene activation in development and disease. Dev. Cell *55*, 84–96.

Sabari, B.R., Dall'Agnese, A., Boija, A., Klein, I.A., Coffey, E.L., Shrinivas, K., Abraham, B.J., Hannett, N.M., Zamudio, A.V., Manteiga, J.C., et al. (2018). Coactivator condensation at super-enhancers links phase separation and gene control. Science *361*. eaar3958–eaar3917.

Sadowski, I., Ma, J., Triezenberg, S., and Ptashne, M. (1988). GAL4-VP16 is an unusually potent transcriptional activator. Nature *335*, 563–564.

Schneider, N., Wieland, F.G., Kong, D., Fischer, A.A.M., Hörner, M., Timmer, J., Ye, H., and Weber, W. (2021). Liquid-liquid phase separation of light-inducible transcription factors increases transcription activation in mammalian cells and mice. Sci. Adv. *7*, eabd3568.

Shelansky, R., and Boeger, H. (2020). Nucleosomal proofreading of activator-promoter interactions. Proc. Natl. Acad. Sci. USA *117*, 2456–2461.

Shin, Y., Berry, J., Pannucci, N., Haataja, M.P., Toettcher, J.E., and Brangwynne, C.P. (2017). Spatiotemporal control of intracellular phase transitions using light-activated optoDroplets. Cell *168*, 159–171.e14.

Shin, Y., and Brangwynne, C.P. (2017). Liquid phase condensation in cell physiology and disease. Science *357*, eaaf4382.

Shrimp, J.H., Grose, C., Widmeyer, S.R.T., Thorpe, A.L., Jadhav, A., and Meier, J.L. (2018). Chemical control of a CRISPR-Cas9 acetyltransferase. ACS Chem. Biol. *13*, 455–460.

Shrinivas, K., Sabari, B.R., Coffey, E.L., Klein, I.A., Boija, A., Zamudio, A.V., Schuijers, J., Hannett, N.M., Sharp, P.A., Young, R.A., et al. (2019). Enhancer features that drive formation of transcriptional condensates. Mol. Cell *75*, 549–561.e7.

Soetaert, K., and Meysman, F. (2012). Reactive transport in aquatic ecosystems: rapid model prototyping in the open source software R (vol 32, pg 49, 2012). Environ. Modell. Softw. *35*, 194.

Soto, L.F., Li, Z., Santoso, C.S., Berenson, A., Ho, I., Shen, V.X., Yuan, S., and Fuxman Bass, J.I. (2022). Compendium of human transcription factor effector domains. Mol. Cell *82*, 514–526.

Sprague, B.L., Müller, F., Pego, R.L., Bungay, P.M., Stavreva, D.A., and McNally, J.G. (2006). Analysis of binding at a single spatially localized cluster of binding sites by fluorescence recovery after photobleaching. Biophys. J. *91*, 1169–1191.

Trojanowski, J., Rademacher, A., Erdel, F., and Rippe, K. (2019). Light-induced transcription activation for time-lapse microscopy experiments in living cells. Methods Mol. Biol. *2038*, 251–270.

Wei, M.T., Chang, Y.C., Shimobayashi, S.F., Shin, Y., Strom, A.R., and Brangwynne, C.P. (2020). Nucleated transcriptional condensates amplify gene expression. Nat. Cell Biol. *22*, 1187–1196.

Wong, F., and Gunawardena, J. (2020). Gene regulation in and out of equilibrium. Annu. Rev. Biophys. *49*, 199–226.

Yang, X.D., Tajkhorshid, E., and Chen, L.F. (2010). Functional interplay between acetylation and methylation of the RelA subunit of NF-kappaB. Mol. Cell. Biol. *30*, 2170–2180.

Zalatan, J.G., Lee, M.E., Almeida, R., Gilbert, L.A., Whitehead, E.H., La Russa, M., Tsai, J.C., Weissman, J.S., Dueber, J.E., Qi, L.S., et al. (2015). Engineering complex synthetic transcriptional programs with CRISPR RNA scaffolds. Cell *160*, 339–350.

Zhang, Y., Brown, K., Yu, Y., Ibrahim, Z., Zandian, M., Xuan, H., Ingersoll, S., Lee, T., Ebmeier, C.C., Liu, J., et al. (2021). Nuclear condensates of p300 formed though the structured catalytic core can act as a storage pool of p300 with reduced HAT activity. Nat. Commun. *12*, 4618.

STAR★METHODS

KEY RESOURCES TABLE

REAGENT or RESOURCE	SOURCE	IDENTIFIER
Antibodies		
Rabbit polyclonal anti-H3K27ac	Abcam	ab4729, lot GR183922-1, RRID AB_2118291
Rabbit polyclonal anti-RNA Pol II CTD	Abcam	ab26721, lot GR3305785-3, RRID AB_777726
Rat monoclonal anti-RNA Pol II S5P	Active Motif	61085, lot 16513002, RRID AB_2687451
Goat anti-rabbit Alexa 633	Thermo Fisher Scientific	A21071
Goat anti-rabbit Alexa 647	Thermo Fisher Scientific	A21244
Goat anti-rat Alexa 647	Thermo Fisher Scientific	A21247
GFP-nanobody Alexa 647	Chromotek	gb2AF647, lot 003192-01-02
Biological samples		
U2OS 2-6-3 cell line	David Spector	https://www.doi.org/10.1016/s0092-8674(04)00171-0
HeLa TRIPZ-ΔshRNA	This manuscript	N/A
Chemicals, peptides, and recombinant proteins		
Janelia Fluor 646 Halo-tag ligand	Promega	GA1120
(+)-JQ1	Sigma-Aldrich	SML1524
Doxycycline	Sigma-Aldrich	D9391
Critical commercial assays		
X-tremeGENE 9 DNA transfection reagent	Roche	6365787001
Qiazol lysis reagent	Qiagen	79306
SYBR Green PCR master mix	Applied Biosystems	4308155
Click-IT RNA imaging kit	Invitrogen	C10329
Deposited data		
Microscopy source images	Mendeley data	https://www.doi.org/10.17632/m97ncz6ryj.1
Software and algorithms		
R software environment	R project for statistical computing	https://www.R-project.org/
EBImage R package	https://bioconductor.org/packages/release/bioc/html/EBImage.html	https://www.doi.org/10.1093/bioinformatics/btq046
NSSQ R package	This study, https://doi.org/10.1007/978-1-4939-9674-2_17	https://www.doi.org/10.5281/zenodo.6357122
NSQFRAP R package	This study	https://www.doi.org/10.5281/zenodo.6357084
FIJI/ImageJ	https://imagej.net	https://www.doi.org/10.1038/nmeth.2089
Fusion software 2.3	Andor Technology	https://andor.oxinst.com/downloads/view/fusion-release-2.3
ThunderSTORM	https://github.com/zitmen/thunderstorm	https://www.doi.org/10.1093/bioinformatics/btu202

RESOURCE AVAILABILITY

Lead contact

Further information and requests for resources and reagents should be directed to the corresponding author Karsten Rippe (karsten.rippe@dkfz.de).

Materials availability

Plasmids generated in this study have been deposited to Addgene at https://www.addgene.org/Karsten_Rippe/.

Data and code availability

- Original microscopy images reported in the figures have been deposited at Mendeley data at the DOI listed in the key resources table. Additional data reported in this paper are available from the lead author upon request.
- The software for image and FRAP analysis is available via GitHub at https://github.com/RippeLab/ and the DOIs listed in the key resources table.
- Additional information required to reanalyze the data reported in this paper is available from the lead contact upon request.

EXPERIMENTAL MODEL AND SUBJECT DETAILS

Cell lines

The U2OS 2-6-3 female osteosarcoma cell line with a *lac*O/*tet*O reporter gene array has been constructed and described previously (Janicki et al., 2004). The HeLa TRIPZ-ΔshRNA cell line (Figure S5B) was generated by stable transfection with the pTRIPZ lentiviral vector (Horizon Discovery) from which the shRNA part had been removed. The cell line expresses rTetR-VP16, which induces red fluorescent protein (turboRFP) upon addition of doxycycline. Cell line identity and absence of contaminations was confirmed by single nucleotide polymorphism (SNP) typing (Muliplexion, Germany; 100% identity, no cross-contamination). Furthermore, the cell lines were tested for the absence of mycoplasma with the VenorGeM Advance kit (Minerva Biolabs).

METHOD DETAILS

Plasmids

Protein constructs were expressed with a CMV promoter using pEGFP-C1/N1 (Clontech) (enhanced GFP, referred to here as GFP) or pcDNA3.1 (Invitrogen) vector backbones (Table S2). Plasmids expressing sgRNAs with 2xPP7 loops targeting *lac*O/*tet*O repeats were designed as gBlocks (Integrated DNA Technology) and cloned into a U6 promoter-driven sgRNA expression vector (Table S3). Plasmids expressing mutated sgRNAs were derived from the wildtype plasmids by site-directed mutagenesis with primers containing the single nucleotide replacement.

Cell culture

Cells were grown in DMEM (1 g/l glucose, Gibco) without phenol-red supplemented with 10% tetracycline-free fetal calf serum (FCS), penicillin/streptomycin and 2 mM L-glutamine using standard cell culture methods at 37 °C and 5% CO_2. For microscopy analysis, cells were seeded onto 8-well chambered coverglass slides (Nunc Labtek, Thermo Fisher Scientific) at a density of 2×10^4 cells per well. For qRT-PCR, 3×10^5 cells were seeded in 6-well plates. One day after seeding, the medium was replaced with imaging medium (Fluorobrite, Gibco, A1896701; 10 % tet-free FCS; penicillin/streptomycin; 2 mM L-glutamine) and cells were transfected using the Xtreme-Gene 9 reagent (Roche) according to the manufacturer's guidelines. An amount of 200–400 ng plasmid DNA and 0.6 μl transfection reagent in 20 μl Optimem (Gibco) were used per well for microscopy experiments. The plasmid DNA mix consisted of 100 ng of guide RNA plasmid and 100 ng of equal amounts of the remaining constructs. For transfections without guide RNA plasmid the 200 ng were split equally among the plasmids. Transfection reactions were scaled up to 2 μg plasmid DNA per well for qRT-PCR experiments. Cells were protected from light until the start of experiments for FRAP and induction time course experiments with light-responsive constructs. Experiments were conducted 24 hpost-transfection except for the FRAP experiments, which were done after 48 h. Cells transfected with the Halo-tag plasmid were labeled in the dark with medium containing 200 nM Janelia Fluor 646 Halo-tag ligand for one hour, followed by three medium washes for five minutes. For the radial profile microscopy experiments or qRT-PCR of light-inducible activator constructs, cells were illuminated by diffuse white LED light for 24 h. rTetR activator constructs were allowed to bind in presence of 5 μg/mL doxycycline (Sigma-Aldrich, D9891), which was added after transfection.

RNA isolation and qRT-PCR

Total RNA was isolated using Qiazol lysis reagent (Qiagen), followed by one round of chloroform extraction and isopropanol precipitation. The purified RNA was treated for 30 min at 37°C with RQ1 DNase (Promega) according to the manufacturer's protocol and then purified using one round of each phenol/chloroform and chloroform extraction followed by precipitation using ethanol in presence of 300 mM sodium acetate pH 5.5 and Glycoblue coprecipitant (Thermo Fisher Scientific). RNA concentration and purity were determined by absorbance measurement. Per sample, one microgram of DNase-treated RNA was used as input for cDNA synthesis using the Superscript IV reverse transcriptase protocol (Thermo Fisher Scientific). qRT-PCR was carried out in technical triplicates with 2 μl of 1:40-diluted cDNA per 10 μl reaction using SYBR Green PCR master mix (Applied Biosystems) with a final primer concentration of 500 nM. The following PCR primers (Eurofins Genomics) were used. Human beta-actin fwd: 5'-TCC CTG GAG AAG AGC TAC GA-3', rev: 5'-AGC ACT GTG TTG GCG TAC AG-3'; VPR-VP16 fwd: 5'- AAG AAG AGG AAG GTT GCC CC-3', rev: 5'-CCC CAG GCT GAC ATC GGT-3'; CFP-SKL fwd: 5'-GTC CGG ACT CAG ATC TCG A-3', rev: 5'-TTC AAA GCT TGG ACT GCA GG-3'. The qRT-PCR analysis was carried out using the $2^{-\Delta\Delta CT}$ method. Reporter RNA expression levels (CFP-SKL) were normalized to beta-actin mRNA levels (ΔCT) and then expressed as fold-change of the mock control.

Microscopy instrumentation

Light-induced time course and most FRAP experiments were carried out with an AxioObserver Z1 widefield microscope (Zeiss) equipped with a 20x air objective (Zeiss Plan-Apochromat 20x/0.8 M27), the ZEN pro 2012 software including modules for z-stack, time-lapse and multi-position acquisition and an Axiocam MRm Rev.3 monochrome camera with filter sets with excitation bandpass, beam splitter, emission bandpass wavelength: GFP, 470/40 nm, 495 nm, 525/50 nm; tdTomato, 535/30 nm, 570 nm, 572/25 nm and mCherry, 550/25 nm, 590 nm, 629/62 nm. SRRF (Gustafsson et al., 2016), dSTORM (Heilemann et al., 2008) and image data acquisition of radial enrichment profiles were conducted with an Andor Dragonfly 505 spinning disc microscope equipped with a Nikon Ti2-E inverted microscope and 40x oil immersion (CFI Plan-Fluor 40x Oil 1.30/0.20, Nikon) and 100x silicone immersion (CFI SR HP Apochromat Lambda S 100x, Nikon) objectives. Multicolor images were acquired using laser lines at 405 nm (tagBFP), 488 nm (GFP), 561 nm (tdTomato and mCherry) and 637 nm (Alexa 633) for excitation with a quad-band dichroic unit (405, 488, 561, 640 nm) and corresponding emission filters of 450/50 (tagBFP), 525/50 (GFP), 600/50 (tdTomato, mCherry) and 700/75 nm (Alexa 633) and an iXon Ultra 888 EM-CCD camera. Live cell experiments were conducted in an incubation chamber (Okolab) at 5% CO_2 and 37 °C temperature. For spot bleaching at 473 nm in FRAP experiments the microscope was extended with an UGA40 70 mW laser scanning system (Rapp Optoelectronic). A Leica TCS SP5 II confocal microscope (Leica) equipped with a 63x Plan-Apochromat oil immersion objective was used for additional FRAP experiments and for measuring recruitment/dissociation kinetics.

High resolution imaging (SRRF and dSTORM)

Imaging was performed on the Andor Dragonfly microscope with a 100x silicone immersion objective and a 2x magnification lens to ensure oversampling. Cells were transfected with the array marker tdTomato-LacI and PHR-GFP-VPR directed to the *tet*O sites by CIBN-rTetR. At 24 h after transfection cells were exposed to doxycycline for 15 min in the dark, illuminated for 10 min by diffuse white LED light and fixed with 4% paraformaldehyde for 10 min and washed with PBS before imaging. 200 frames were acquired per channel in spinning disc mode for one super-resolved SRRF image. Exposure time was 2.5 ms with 100% laser intensity of the 488 nm laser for GFP. SRRF analysis was performed using the SRRF-stream tool implemented in the microscope software with 5 x 5 sub-pixels, a ring radius of 1.5 pixels for radiality calculations and mean-projection of radiality images. For dSTORM imaging cells transfected with PHR-GFP-VPR, CIBN-rTetR and tdTomato-LacI after illumination and fixation were immunostained with an Alexa 647 conjugated GFP-nanobody (1:500, Chromotek) according to the manufacturer's protocol. Cells were imaged in a reducing oxygen scavenging buffer containing 10% glucose (wt/v), 10mM Tris (pH 8.0), 2x SSC, 37 μg/ml glucose oxidase (Sigma, G2133), 1% (v/v) catalase (Sigma C3515) and 140 mM β-mercaptoethanol. 2000 frames were acquired in widefield mode with a power density illumination lens PD3, full intensity of the 637 nm laser and 50 ms exposure time. Image series were analyzed with the ThunderSTORM plugin in ImageJ (Ovesny et al., 2014). The analysis comprised image filtering by a B-spline wavelet filter, approximate localization of molecules using the local maximum algorithm and sub-pixel localization by fitting an integrated gaussian (6 pixel radius). The resulting localization accuracy was 32 nm on average after excluding outliers. dSTORM images were created by normalized Gaussian rendering with five-fold magnification and 20 nm lateral uncertainty.

Droplet fusion videos and half-spot FRAP

Exchange of proteins within the reporter array was assessed by bleaching half of the locus and evaluating the recovery between the unbleached and bleached part (Erdel et al., 2020). Image series of half-spot FRAP recoveries and optodroplet fusion events in living cells were recorded using the FRAP wizard on a Leica SP5 confocal microscope equipped with a 63x oil immersion objective. Cells were illuminated at 488 nm for 2–5 minutes before acquiring image series for up to 10 min (or for 30 s for half-spot FRAP) at 0.1s time intervals using a scan area of 512x64 pixels. Reporter spots were identified by the co-transfected tdTomato-LacI marker. Bleaching was done as point bleach next to the array spot at full laser intensity.

Light-induced time course experiments

Light-induced time course experiments followed a previously published protocol (Trojanowski et al., 2019) and were conducted with the Axio-observer Z1 widefield microscope. Slides with transfected cells were kept in the dark until the start of image acquisition and red-light illumination was used during sample preparation before initiating the reaction with blue light. For JQ1 (Sigma-Aldrich, SML1524) treatment the drug was diluted in medium and added to the respective wells to a final concentration of 1 μM three hours before the start of imaging. Doxycycline (Sigma-Aldrich, D9891) was added 15 minutes before imaging to a final concentration of 5 μg/ml in the dark to induce binding of CIBN-rTetR. The focal plane was determined by red-filtered transmitted light and kept constant by the hardware autofocus. Imaging time courses comprised repeated cycles of imaging of a grid of 16 positions (4x4, 50% negative overlap) with three z-slices (distance 1.0 μm) in intervals of 2 minutes over 90 minutes or 60 minutes for BRD4 recruitment experiments. After each time course experiment the slide was exchanged with a slide that had been stored in the dark to ensure that between experiments PHR molecules that had been exposed to stray light from a neighboring well had reverted to their inactive conformation in the dark.

Analysis of time course images

Images were processed with the EBImage and NSSQ R packages as described previously (Trojanowski et al., 2019). In a first step, positions of nuclei with successful recruitment of PHR-GFP-AD were manually selected and segmented in the GFP channel by

automated local thresholding for each time point. The nucleus was tracked by mapping the segmented objects with minimal distance in consecutive frames. The best focal plane was selected from the z-stack for each time point using the intensity gradient inside the nucleus area. The reporter gene locus was segmented inside the nuclear area using a quantile-based threshold in the PHR-GFP-AD channel. The spot position was tracked through the time course by finding the closest segmented object in consecutive images. The areas of spot (A_{spot}) and nucleus masks ($A_{nucleus}$) and the average intensities inside the spot (I_{spot}), nucleus ($I_{nucleus}$) and ring-shaped background regions around them (I_{spotbg}, $I_{nucleusbg}$) were measured in each channel. The amount of fluorescence intensity recruited to the reporter spot was then calculated as the product of background subtracted spot intensity and area:

$$I_{enriched}(t) = \left(I_{spot} - I_{spotbg}\right) \cdot A_{spot}$$

Segmented image series were manually curated by removing cells with morphological abnormalities, missing expression or segmentation errors and then classified as responders or non-responders based on visible accumulation of intensity in the reporter spot in the reader channel. To account for the short time shift of acquisition between positions in one imaging cycle, the intensity values at the beginning of each cycle were calculated by linear interpolation. The resulting single cell time courses were then either directly averaged for each time point to yield absolute intensity values or normalized by subtracting the initial value and dividing by the maximum value before averaging:

$$I_{norm}(t) = \left(I_{enriched}(t) - I_{enriched}(0) \right) / max\left(I_{enriched}(t) - I_{enriched}(0)\right)$$

Averaging was performed either for all cells or only for responder cells. The first value was subtracted so that all curves started at an intensity value of zero. For BRD4 recruitment time courses time traces were normalized to their maximum values without subtraction of the first time point. The value of the first time point was then subtracted after averaging. Times to half-activation were determined from single cell time courses as the first time point, at which the normalized intensity equaled or exceeded 0.5. The responder fraction was calculated as the number of cells annotated as responders divided by the total number of cells remaining after manual curation. Time course maximum values were determined as the average plateau value of tdMCP-tdTomato intensity over the last five time points.

Light-induced optodroplet formation

Image series of cells transfected with combinations of PHR-GFP-AD and CIBN-rTetR, CIBN-dCas9-CIBN or dCas9 + tdPCP-CIBN were acquired with the same settings as the induction time course experiments over 6 cycles at 25 positions. For experiments with CIBN-rTetR, doxycycline was added 15 minutes before imaging. Variations of nuclear intensity were computed after removing the contribution of the reporter array by manually selecting the spot and applying a circular mask with 7 pixels diameter. Mean and standard deviation of intensities in the processed nucleus images and in a ring-shaped background area around the nucleus were determined. Subsequently, image series were manually curated and classified as containing optodroplets or not by checking for the presence of spherical structures outside the reporter spot. For quantification, optodroplets inside the nucleus were segmented using the median of the nuclear intensity multiplied by 1.75 as a segmentation threshold. The droplet abundance was determined as the area of segmented droplets normalized to the nucleus area. The critical value for droplet formation was determined as the nuclear intensity at which the relative droplet area exceeded an empirically determined threshold of 1%. This threshold yielded a good agreement with the manual annotation of cells as droplet containing or not. To represent the relative droplet area as a smooth function of the nuclear intensity, we fitted a logistic function to it:

$$D(c) = A + B/(1 + exp(-k \cdot (c - c_0))),$$

where $D(c)$ is the droplet abundance, c the nuclear concentration and the remaining free fitting parameters are offset A and amplitude B. The intensity at which this function crosses 1% corresponds to the critical value.

FRAP analysis

FRAP experiments were carried out on the Zeiss widefield microscope described above with an external micromanipulation laser for bleaching. This set-up allowed fast acquisition of time courses for a large number of cells at different conditions and yielded results similar to those obtained with a confocal microscope (Figures S4A–S4C). Laser position calibration was performed according to the UGA40 software instructions on a fluorescent calibration slide. Conditions with optogenetic constructs were illuminated for at least one minute in the GFP channel to saturate binding to CIBN before carrying out FRAP. The reporter spot was manually selected as bleach region and bleached at 100 % laser intensity for one second, 3–4 frames after starting an imaging time series of four minutes with one second intervals (on-spot bleach). For determining construct-specific diffusion coefficients, a central nuclear bleach region outside of the reporter spot was bleached and fluorescence recovery was monitored at 300 ms intervals for one minute (off-spot bleach). FRAP of *tet*O-bound dCas9-GFP-VPR with sgRNA-wt and sgRNA-mut was carried out with the same settings but with an alpha Plan-Apochromat 100x/1.46 Oil DIC M27 objective (Zeiss). The spot or bleach region intensities in the image series were quantified by a semi-automated analysis pipeline with our *R* software package NSQFRAP and normalized to pre-bleach and nuclear intensity to account for bulk bleaching. Normalized recovery curves were fitted with a reaction-diffusion model for clustered binding sites (Sprague et al., 2006) using the empirical post-bleach profile as an initial condition and the effective diffusion coefficient determined from the off-spot FRAP measurements (Figure S4D). The confocal FRAP experiments were conducted as described previously

(Muller-Ott et al., 2014) on the Leica SP5 microscope using the Leica LAF software and bleaching with the argon laser lines (458 nm, 476 nm, 488 nm, 496 nm). Images of 128×128 pixel with zoom factor 9 corresponding to 194 nm/pixel were recorded at 1400 Hz line frequency resulting in a frame time of 115 ms. For each cell, 70 pre-bleach and 2 bleach frames were recorded with a 1 μm diameter circular bleach region. It was placed on the reporter array ("on spot") or elsewhere in the nucleus but outside nucleoli ("off spot"). Subsequently, 1200 (on spot) or 300 (off spot) post-bleach frames were recorded (Figures S4A–S4C).

Comparison of FRAP for widefield and confocal microscopy setup

The widefield FRAP used in our study provides fast data acquisition with imaging being decoupled from bleaching. However, the z-resolution resolution is lower as compared to a confocal microscope setup. We thus compared GFP-LacI diffusion and binding to the reporter array in FRAP experiments with the widefield FRAP system to measurements with a Leica SP5 confocal microscope (Leica, Germany) equipped with a 63x Plan-Apochromat immersion objective. Image analysis and parameter estimation were done as for widefield FRAP with the following adaptations: The post-bleach intensity profiles were not fitted individually but averaged, the estimated bleach profile parameters were applied globally to calculate initial conditions and the fitting range of the correction factor *bgRatio* was set between 0.3 and 2.3. A fit of the data to a reaction-diffusion model yielded similar values for the two different FRAP setups of D_{eff} = 2.3 μm^2/s and k_{off} = 0.012 s^{-1} (widefield) vs. D_{eff} = 3.3 μm^2/s and k_{off} = 0.010 s^{-1} (confocal) (Figure S4B and S4C). The widefield curves recovered to higher values in the first seconds and then showed a similar behavior as the confocal FRAP curves but with a lower immobile fraction (widefield: 9.9 %, confocal: 29 %). These differences can be rationalized by the higher z-resolution of the confocal setup that reduces the number of freely diffusive molecules observed below and above the reporter array, which do not contribute to a potential immobile fraction. Moreover, shorter FRAP time courses were recorded with the confocal system due to higher imaging related bleaching and out-of-focus movement of the reporter array. Potentially, this shorter observation time in confocal mode may lead to higher estimates of the immobile fraction.

Quantification of images for FRAP analysis

Intensities in the region of interest were determined automatically using functions of the NSSQ (Trojanowski et al., 2019) and EBImage (Pau et al., 2010) packages in R (R Core Team, 2020) and the bleached nucleus was segmented by local thresholding (Figure S4D). As dCas9-GFP was depleted in the nucleus, images were blurred and the whole cell was segmented for this construct. For on-spot experiments the reporter array was segmented in the first pre-bleach frame using the 98% quantile inside the nucleus. The bleach region was segmented in an image created from the difference of pre-bleach and first post-bleach frame. To correct for chromatin or cell movements the nucleus was tracked, and positions of spot and bleach region mask were shifted accordingly. If automated tracking failed, spot positions were selected manually in every tenth frame and all masks were shifted accordingly. Average intensities were extracted for each time point in the nucleus, in a ring-shaped area around the nucleus (background intensity), in the spot area and in a ring-shaped area around the spot (local background). The intensity profile around the center of the bleach position was measured as the median intensity of rings starting with a radius of 1 pixel up to a radius of 9 pixels (20x objective) or 40 pixels (100x objective). The pixel size was 0.63 μm (20x objective) or 0.13 μm (100x objective) based on a reflective calibration slide with a grid of known size. Recovery curves of profiles and average intensities were subjected to the following normalizations: Background I_{nuc_bg} in a region around the nucleus was subtracted and intensity profiles $I(r,t)$ were normalized to the average nuclear intensity I_{nuc} to account for the overall reduction of fluorescence signal during the experiment. The intensity of the center position of the first post-bleach frame $I(r=r_{center}, t=0)$ was subtracted. The resulting profile was normalized to the average value before bleaching for each profile position r.

$$I_1(r,t) = I(r,t) - I_{nuc\_bg}(t)$$

$$I_{nuc\_norm}(t) = I_{nuc}(t) - I_{nuc\_bg}(t)$$

$$I_2(r,t) = \frac{I_1(r,t)}{I_{nuc\_norm}(t)}$$

$$I_3(r,t) = I_2(r,t) - I_2(r = r_{center}, t = 0)$$

$$I_{norm}(r,t) = \frac{I_3(r,t)}{mean(I_3(r,t<0))}$$

For off-spot experiments the average bleach region intensity was calculated from normalized profiles by averaging intensities from the region center to a radius of 3.5 μm weighted by the pixel number in each ring of the profile and leaving out the innermost value. For quantitating the spot intensity, the nuclear background signal was subtracted. Average spot intensities were normalized by dividing them by the average nucleus intensity, subtracting the minimum value in the first post-bleach frame and dividing by the average pre-bleach value.

$$I_{spot,1}(t) = I_{spot}(t) - I_{nuc\_bg}(t)$$

$$I_{nuc\_norm}(t) = I_{nuc}(t) - I_{nuc\_bg}(t)$$

$$I_{spot,2}(t) = \frac{I_{spot,1}(t)}{I_{nuc\_norm}(t)}$$

$$I_{spot,3}(t) = I_{spot,2}(t) - min(I_{spot,2}(t))$$

$$I_{spot,norm}(t) = \frac{I_{spot,3}(t)}{mean(I_{spot,3}(t<0))}$$

Segmented image series were manually curated by removing cells where (i) segmentation or tracking failed, (ii) the normalized spot intensity exceeded 1.2, (iii) the spot intensity was less than 25% above background, or (iv) the recovery curve displayed strong intensity jumps.

Theoretical framework for FRAP analysis of clustered binding sites

Recovery of fluorescence intensity inside the spot area was modeled by a localized cluster of binding sites b inside a cylindrical volume of radius r_s that can be bound by freely diffusing particles f to form a complex c according to the theoretical framework established previously (Sprague et al., 2006):

$$for\ r \leq r_s:$$

$$\frac{\partial f(r,t)}{\partial t} = D_{eff} \cdot \nabla_r^2 f(r,t) - k_{on}^* \cdot f(r,t) + k_{off} \cdot c(r,t)$$

$$\frac{\partial c(r,t)}{\partial t} = k_{on}^* \cdot f(r,t) - k_{off} \cdot c(r,t)$$

$$for\ r > r_s:$$

$$\frac{\partial f(r,t)}{\partial t} = D_{eff} \cdot \nabla_r^2 f(r,t)$$

$$c = 0$$

Here, D_{eff} is the effective diffusion coefficient that includes free diffusion and transient non-specific binding to chromatin. The apparent rate k_{on}^* for binding to cluster sites includes the equilibrium concentration of free cluster binding sites. We extended this description by using a bleach region that can be larger than the spot area and modeled the initial conditions by a Gaussian function with a central plateau. It accounts for diffusion during the time between bleaching and the first post-bleach frame.

$$I(r < r_p, t = 0) = 0$$

$$I\ (r \geq r_p, t = 0) = A \cdot \left(1 - e^{\frac{-(r-r_p)^2}{\sigma}}\right)$$

In this equation, r_p is the plateau radius, A the intensity of the unbleached peripheral region and σ describes the width of the Gaussian. The binding site cluster was approximated as a cylinder with a homogeneous distribution of binding sites in z-direction at the center of a cylindrically shaped nucleus. This allowed us to formulate the system of partial differential equations in polar coordinates. For the estimation of diffusion coefficients from off-spot FRAP experiments we used a simplified model with only a diffusive and an unspecific immobile fraction.

$$\frac{\partial f(r,t)}{\partial t} = D_{eff} \cdot \nabla_r^2 f(r,t)$$

The time evolution of intensity profiles was simulated by solving the PDE system numerically using the R-package ReacTran (Soetaert and Meysman, 2012) that implements finite-difference grids. The radial axis from the spot center to the nucleus radius was split into 50 intervals to yield 50 concentric grid cells. A single ring-shaped grid cell was used for each radial interval assuming symmetry around the central spot position. Fluxes at the boundaries were set to zero. The model simulation resulted in radial profiles that were converted to averaged intensity values. The intensity in an area up to a radius of 3.5 μm for the pure diffusion model and from 0.0 to 1.0 μm for the reaction-diffusion model was averaged with the method described above for the image data.

Parameter estimation from recovery curves

We used individual recovery curves from off-spot FRAP measurements to estimate D_{eff} of the ligand constructs. The nuclear radius was determined from the segmented nuclear mask. The initial profile of free diffusible molecules $f(r,t{=}0)$ was estimated from the normalized profile of the first post-bleach frame fitted by a Gaussian with a plateau diameter of r_p and the parameter σ describing the gaussian width. The amplitude was set to 1. Recovery of the normalized intensity in the bleach region was then fitted by a diffusion-only model with an immobile fraction using the *nls* function in R with multiple start values for the fit parameters. Starting values were varied between D_{eff} = 0.1 and 5 $\mu m^2/s$ and an immobile fraction f_i = 0.1 and 0.5. The best fit out of all starting values was selected. The median of D_{eff} across single cell recovery curves for each ligand-target combination was used for further analysis. The normalized on-spot recovery curves were used to calculate k_{off} and immobile fraction of molecules at the binding site cluster. The immobile fraction f_i was determined by fitting the data to a single exponential to the mostly binding dominated part of the recovery curve after 30 seconds:

$$I(t|t>30s) = A + B\cdot\left(1 - e^{-k\cdot t}\right)$$

The immobile fraction was calculated as

$$f_i = 1 - A - B$$

with $f_i \leq 0.5$. The full recovery time course was then fitted with the localized binding site cluster model with D_{eff} and f_i fixed. An approximated start value of the pseudo on-rate k^*_{on} was calculated using the ratio of the maximum spot and the nucleus intensity before bleaching:

$$spotRatio_{apparent} = \frac{median\left(I_{spot,\ max}(t<0) - I_{spot\_bg}(t<0)\right)}{median\left(I_{spot\_bg}(t<0)\right)}$$

The *spotRatio* parameter was corrected for the immobile fraction which was estimated from the fractional recovery at the last five time points:

$$spotRatio = spotRatio_{apparent}\cdot(1 - f_i) - f_i$$

In (pre-bleach) equilibrium the ratio of bound and free molecules in the spot is given by $c/f = k^*_{on}/k_{off}$, so that k^*_{on} can be calculated as

$$k^*_{on} = \frac{c}{f}\cdot k_{off} = spotRatio\cdot k_{off}$$

A correction factor *bgRatio* that is multiplied with *spotRatio* was introduced as a free fit parameter to adjust for differences in the ratio of free and bound fraction. The initial profile $f(r,t{=}0)$ was estimated as described for the off-spot experiments and $c(r \leq r_s, t{=}0)$ was set to 0. Model simulations for a given parameter set yielded radial profiles of free and bound molecules *f(r,t)* and *c(r,t)* for each timepoint. These were processed and normalized like the imaging intensities:

$$y_{norm}(r,t) = (1 - f_i)\cdot\frac{f(r,t) + c(r,t)}{f(r,t = 240s)\cdot(1 + spotRatio\cdot bgRatio)}$$

This normalized profile was integrated from the spot center to 1.0 μm yielding a normalized time course $y_{norm}(t)$ that could be fitted to the data. The recovery curves were fitted by minimizing the sum of squared residual on a grid of parameter values for k_{off} and *bgRatio* as described previously (Sprague et al., 2006). First, k_{off} values were varied between 10^{-4} and 0.1 s^{-1} in seven steps and *bgRatio* between 0.5 and 2 in steps of 0.21. The best parameter pair was used as a starting point for a refined optimization. In this second optimization the value of k_{off} was multiplied by a factor between 0.2 and 8 and *bgRatio* was varied in steps of 0.1. The parameter pair with the smallest sum of squared residuals was selected as the best fit. Fits with obvious systematic deviations from the data points were manually sorted out. Residence times were limited to the maximum observation time or reported as outside the observation time.

Model for TF residence time dependent activation

The experiments conducted with dCas9 activators targeted with wildtype vs mutated guide RNA activator (Figures 7A–7G) revealed large differences of transcriptional activation for different residence times that were independent of binding site occupancy. A kinetic model of transcriptional activation (Figure 7H) shows how these differences in residence times become functionally relevant if a kinetic proof-reading mechanism is present that contains an energy-dissipating step subsequent to DNA binding like nucleosome remodeling or posttranslational modifications of the transcription complex or the TF itself (Hopfield, 1974; Kurosu and Peterlin, 2004; Shelansky and Boeger, 2020; Wong and Gunawardena, 2020; Yang et al., 2010). Such a mechanism in generic form is depicted in Figure 7H where the TF binds with rate constant k_{on} to the free promoter (state *A*) and dissociates from the bound state *B* with rate constant k_{off}. An energy dependent step with rate k_1 leads to an activated TF bound state. The modified TF can dissociate from this state with the same dissociation rate constant k_{off} as in state *B*. RNA is produced only from the activated state *C* with rate constant k_t and is degraded with rate k_m. The total concentration of all promoter states is normalized to one, so that $A + B + C = 1$. The con-

centration of free TF is assumed to be high compared to the concentration of binding sites so that it can be absorbed into a pseudo-binding rate constant $k^*_{on} = k_{on} \cdot [TF]$. Furthermore, the loss of free modified TFs is taken to be comparatively fast so that rebinding of modified TFs can be neglected. The model is then described by the following system of ordinary differential equations:

$$\frac{dB}{dt} = k^*_{on} \cdot (1 - B - C) - (k_{off} + k_1) \cdot B$$

$$\frac{dC}{dt} = k_1 \cdot B - k_{off} \cdot C$$

$$\frac{dR}{dt} = k_t \cdot C - k_m \cdot R$$

The steady state levels are:

$$B = \frac{1}{\left(1 + \frac{k_{off}}{k^*_{on}}\right) \cdot \left(1 + \frac{k_1}{k_{off}}\right)}$$

$$C = \frac{1}{\left(1 + \frac{k_{off}}{k^*_{on}}\right) \cdot \left(1 + \frac{k_{off}}{k_1}\right)}$$

$$R = \frac{k_t}{k_m \cdot \left(1 + \frac{k_{off}}{k^*_{on}}\right) \cdot \left(1 + \frac{k_{off}}{k_1}\right)}$$

The TF concentration can be expressed in units of K_D which leads to the equation for steady state RNA levels plotted in Figure 7H, right:

$$R = \frac{k_t}{k_m \cdot \left(1 + \frac{1}{[TF]}\right) \cdot \left(1 + \frac{k_{off}}{k_1}\right)}$$

The occupancy θ can be determined from the sum of (normalized) states B and C:

$$\theta = B + C = \frac{1}{1 + \frac{k_{off}}{k^*_{on}}} = \frac{[TF]}{[TF] + \frac{k_{off}}{k_{on}}}$$

Both steady state RNA levels and binding site occupancy depend on the TF concentration. The RNA levels are additionally limited by the last term of the denominator that contains the ratio of the TF modification rate constant and the dissociation rate. Hence, the residence time $\tau_{res} = 1/k_{off}$ regulates the steady state RNA level. This is illustrated by setting the modification rate constant to k_1 = 0.005 s^{-1} and comparing two different dissociation rates k_{off} = 0.006 s^{-1} (τ_{res} = 167 s) and k_{off} = 0.014 s^{-1} (τ_{res} = 71 s). These k_{off} or τ_{res} values reflect those observed for dCas9-GFP-VPR targeted to the *tet*O sites by mutated and wild type sgRNA. For simplicity the binding behavior was approximated by a weighted average of the apparent residence time and the immobile fraction f_i, that was assumed to have a residence time equal to the FRAP experiment duration (τ_{res} = 240 s).

$$k_{off} = \frac{1}{(1 - f_i) \cdot \tau_{FRAP} + f_i \cdot 240\ s}$$

The promoter becomes saturated at somewhat higher TF concentrations for the higher k_{off} rate as computed for a value of k_{on} = 10^5 M^{-1} s^{-1}, corresponding to K_d = 60 nM and K_d = 140 nM, respectively (Figure 7H, promoter occupancy plot). Notably, the RNA output is not only dependent on binding site occupancy but also directly reflects k_{off}. This is illustrated by the relation of RNA production and TF concentration given in units of the dissociation constant K_d and thus normalized to the same promoter occupancy (Figure 7H, RNA plot). It can be seen that transcription increases with τ_{res} and the difference between the higher and lower τ_{res} persists even if full occupancy is reached. Thus, TF residence time and not binding site occupancy governs RNA production at saturating TF expression levels.

Analysis of binding and dissociation kinetics

Binding and dissociation time courses were performed on a Leica SP5 confocal microscope. Cells transfected with PHR-mCherry-VP16 and CIBN constructs were imaged using a 594 nm laser line (mCherry) for focusing without triggering the optogenetic components. An image was taken before starting a 2–3 min image series using both the 594 nm and 488 nm laser line for imaging the co-transfected GFP-LacI array marker and triggering PHR-CIBN interaction with time intervals of 6 seconds. After recording this time series, the 488 nm laser line was switched off and 2 μm z-stacks (0.5 μm step-size) of the same positions were recorded for 20-

30 min at 1 min intervals to monitor PHR-CIBN dissociation. The additional recruitment of PHR-GFP-VPR to CIBN-rTetR was recorded in cells with and without droplets the cells were pre-exposed to the 488 nm line during focusing for approximately 60 s before starting the time series acquisition. This led to pre-saturation of the direct binding between PHR and CIBN. Four z-stacks (1.0 μm step-size) were recorded for 10 min at 5 s intervals. Reporter spot tracking and intensity quantification were performed as described for FRAP and using the LacI array marker to identify the reporter spot. Spot intensities were subtracted from the background intensity determined in a ring-shaped area around the spot and normalized for each cell to the last (t = 168 s, binding) or first timepoint (t = 0 s, dissociation and additional recruitment), respectively.

Immunofluorescence

Slide wells with transfected cells that had been illuminated for 24 h or 90 min were washed once with phosphate-buffered saline (PBS) and fixed with 4 % paraformaldehyde in PBS (Sigma-Aldrich, 252549) for 12 minutes. After washing with PBS cells were permeabilized with ice-cold 0.1% Triton-X100 (Merck, 108643) in PBS for 5 minutes. Blocking with 10 % goat serum (Cell Signaling Technology) in PBS for 15 minutes was followed by incubation with primary antibodies in 10 % goat serum for one hour at room temperature (antibodies used: rabbit anti-H3K27ac, 1:1000; rabbit anti-RNA Pol II CTD, 1:1000; rat anti-RNA Pol II S5P, 1:500; key resources table). Cells were washed three times for 5 min with 0.002 % NP40 (Sigma-Aldrich, i8896) in PBS. Incubation with the secondary goat antibodies at a dilution of 1:1000 was done for 30 minutes at room temperature in 10 % goat serum/PBS (anti-rabbit Alexa 633 and 647, anti-rat Alexa 647, see key resources table). Cells were washed twice for 5 min with PBS and stored in PBS at 4 °C until they were imaged on the following day.

Ethynyl-uridine staining

For EU staining transfected cells were labeled in the dark with the Click-IT RNA imaging kit (Invitrogen, C10329) according to the manufacturer's protocol before illumination by diffuse white LED light (90 min in the presence of EU), fixation and staining with Alexa Fluor 647 azide (Thermo Fisher, A10277).

Single molecule RNA FISH

Probes of the RNAScope system (ACD Bio) against the MS2 sequence of the U2OS-2-6-3 reporter cell line covering position 851 to 2163 of the reporter RNA were custom designed by ACD Bio. Slides with transfected cells that had been illuminated for 24 hours were washed once with phosphate-buffered saline (PBS) and fixed with 4% paraformaldehyde in PBS (Sigma-Aldrich, 252549) for 12 minutes. After washing three times with PBS cells were treated with 3% hydrogen peroxide for five minutes, washed with PBS and treated with protease III (ACD Bio) diluted 1:15 for ten minutes, followed by three PBS washes. Hybridization of target and amplification probes was then performed according to the manufacturer's protocol. Target probes after amplification were labelled with Alexa Fluor 488 using the C1 detection kit. Cells were stored and imaged in PBS.

Radial profiles, spot intensities and areas

Cells transfected with light-responsive constructs were cultured for 24 h in the presence of diffuse white LED light after transfection and then subjected to imaging. For the comparison of spot intensities and areas in cells with and without droplets cells were kept in the dark for 24 h and then illuminated for 10 minutes before fixation. For each condition 14 μm z-scans (1 μm step size) on 36–81 positions (6x6 to 9 x 9 grid, 1% overlap) were recorded per well on the with an Andor Dragonfly 505 spinning disc microscope. Images were processed with the NSSQ package (Trojanowski et al., 2019). Nuclei with activator recruitment in the GFP-AD channel or array marker signal were manually selected in maximum projections of each position and then segmented in sum-projected images by local thresholding. Three consecutive z-planes with the highest contrast were mean-projected to yield a single image for quantification. Subsequently, the spot position was selected in each segmented cell based on the co-transfected array marker (tagBFP-LacI or tdTomato-LacI) and a disc shaped spot mask, a ring-shaped background mask and a nuclear mask were used to quantify average intensities in all channels. Spot mask diameters were 1.6 μm (5 pixels) for activators and 3.8 μm (12 pixels) for nascent RNA. Radial profiles were measured by creating masks of concentric rings of pixel-wise increasing radius around the spot position and measuring average intensities up to a radius of 2.9 μm (9 pixels). The minimum value was subtracted from the profiles, and they were divided by the local background intensity for normalization. Single cell profiles were averaged for each condition and the minimum value was subtracted. The resulting enrichment score profile gives qualitative information about the accumulated intensity in the spot center. For quantitative comparisons of local concentrations (occupancy and promoter activity plots), average spot intensities were measured in images acquired on the same day with the same imaging parameters. The average intensity in the spot background region was subtracted from the average spot intensity. The resulting intensity in the activator-GFP channel was normalized to the LacI marker channel. For measurements of spot areas, the spot was segmented by local thresholding creating individual masks for the activator and marker channel. The threshold was manually adjusted for cells in which the segmentation failed. The activator area beyond the marker area was determined for each cell as the difference of the area of the marker spot mask and the activator spot mask.

Image analysis software

The NSSQ package (Trojanowski et al., 2019) for images analysis is available at https://github.com/RippeLab/NSSQ. The *R* software package NSQFRAP for the semi-automated FRAP analysis can be downloaded from https://github.com/RippeLab/NSQFRAP.

QUANTIFICATION AND STATISTICAL ANALYSIS

Mean values and 95% confidence intervals (CI) for time courses of nascent transcripts, BRD4 or fluorescence recovery and for intensity profiles were calculated from single cell data for every time point or radial position from a Student's t-distribution. Pairwise comparisons of the mean for qRT-PCR or relative intensities were done using unpaired, two-sided Student's or Welch's t-tests, respectively. To check for the respective effects of two grouping variables (AD type and presence of optodroplets for half-activation times; occupancy group and sgRNA for the effect of residence time on promoter activation) a two-way ANOVA (type II) was performed. Error bars represent one standard deviation (s. d.) for qRT-PCR experiments and the standard error of the mean (s. e. m.) for half-activation times as indicated. For residence times the mean and CI of k_{off} were determined before calculating the inverse ($1/k_{off}$). Axis breaks were introduced in relative intensity and qRT-PCR plots for conditions with values on very different scales or with outliers and are marked by an interruption of the axis. Box plots show first and third quartile (box), median (bar), data points within 1.5-fold interquartile range (whiskers) and outliers (points). Numbers of cells (n) are reported in Tables S4-9.

Molecular Cell, Volume *82*

Supplemental information

Transcription activation is enhanced by multivalent interactions independent of phase separation

Jorge Trojanowski, Lukas Frank, Anne Rademacher, Norbert Mücke, Pranas Grigaitis, and Karsten Rippe

Supplemental figures

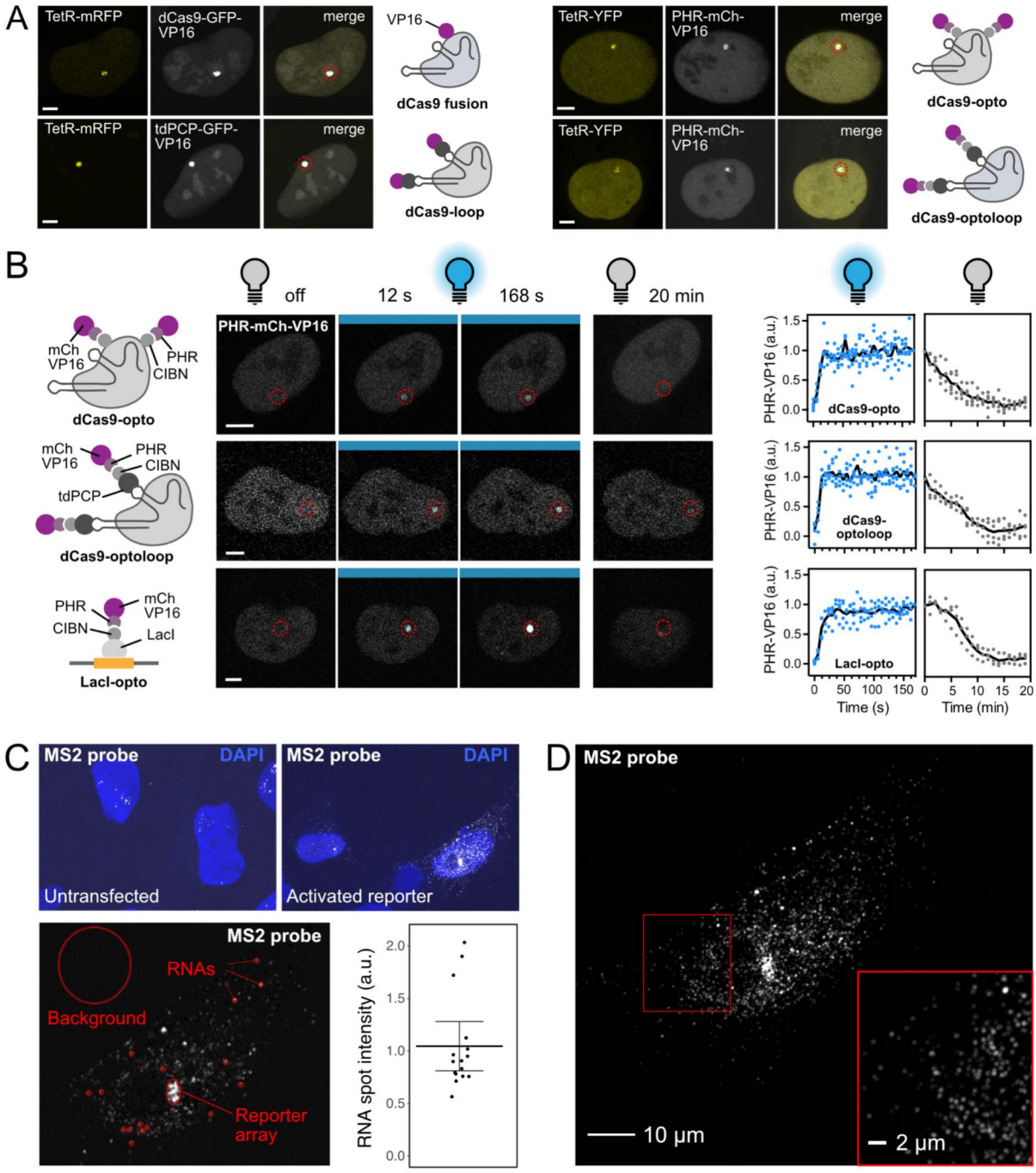

Figure S1. Light-induced binding of TFs and reporter array activation. Related to Fig. 1. (**A**) Confocal images of U2OS 2-6-3 cells expressing dCas9 fusion, dCas9-loop, dCas9-opto and dCas9-optoloop TF constructs recruited to the *lacO* sites of the reporter. The constructs contained VP16 as activation domain (AD). TetR-mRFP/YFP was co-transfected as an array marker (dashed circle). Scale bars, 5 µm. (**B**) Representative images and quantification of the association and dissociation kinetics of optogenetic TF constructs in the presence or absence of blue light. Solid line depicts the intensities averaged over all cells for each timepoint (*n* = 3-

5 cells per condition). Intensities were normalized to the first (association) or last (dissociation) timepoints. Scale bars, 5 µm. (**C**) Single molecule RNA FISH of MS2 reporter RNA visualized by confocal microscopy. Top: comparison of untransfected cells and cells activated by rTetR-opto-VP16 and overnight illumination. Bottom: Single *z*-plane image showing transcripts at the reporter array, in the nucleus and in the cytoplasm. Single RNA spots in the nucleus were selected for quantification (red circles). About 80 nascent RNAs were detected around the array, as estimated by comparison to the intensity of single RNA spots (bottom right). (**D**) Super-resolution radial fluctuations (SRRF) imaging of the same activated cell (maximum intensity z-projection), identifying about ~2000 distinct MS2 RNA spots with ~1400 located in the nucleus and ~600 in the cytoplasm.

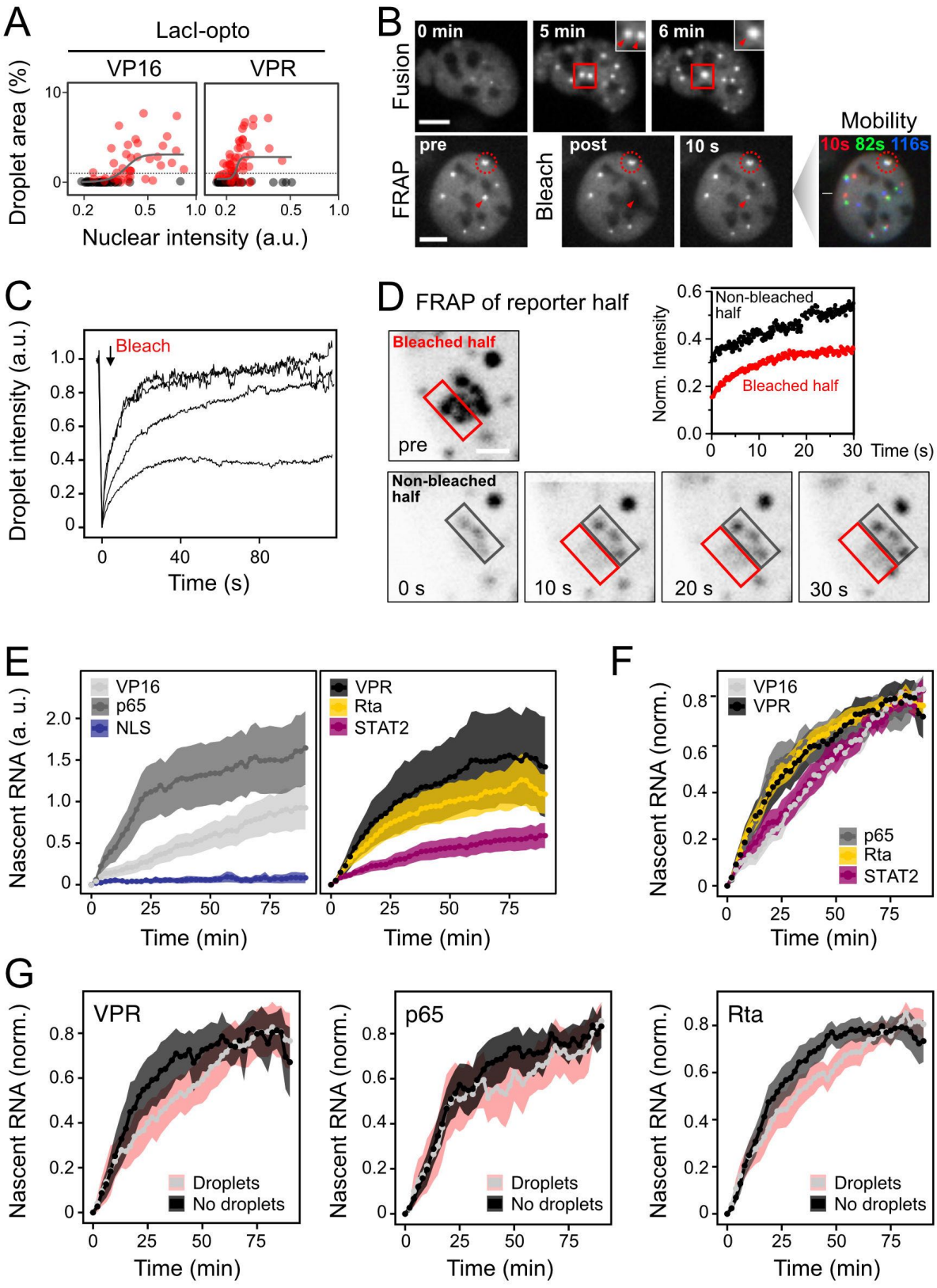

Figure S2. AD droplet formation and transcription activation kinetics. Related to Fig. 3. (**A**) Droplet formation propensities for PHR-VP16 and -VPR recruited via the LacI-opto construct. CIBN-LacI lowers the critical droplet concentration for VP16 (compare **Figure 1D**). (**B**) Liquid-like properties of PHR-VPR droplets. Top: Image series showing the fusion of two

droplets. Bottom: FRAP image series. Droplets recovered mostly within seconds after bleaching (arrow). In contrast to reporter-bound VPR assemblies, droplets also showed displacement from their original position as apparent from their color-coded positions after 10, 82 and 116 s. The reporter array is marked by a dashed circle. Scale bars, 5 µm. (**C**) Individual FRAP recovery curves of PHR-VPR droplets in four different cells. (**D**) Partial bleach experiment of reporter-bound rTetR-opto-p65 in a cell above c_{crit}. The absence of an initial equilibration of fluorescence intensities between the non-bleached and bleached half indicates that there is no preferential internal mixing within the entire reporter-bound assembly. Intensities in the plot are normalized to the pre-bleach frame. Some bleaching also occurs in the non-bleached half of the reporter due to the small size of the TF assembly compared to the bleach laser beam diameter. Scale bar, 1 µm. (**E**) Averaged transcription activation kinetics of combined responder and non-responder cells from the data set depicted in **Figure 3B** (n = 37-132 cells per condition). Ribbon, 95% CI. (**F**) Averaged transcription activation kinetics after normalization to the maximum value of individual trajectories only for responding cells of **Figure 3B**. Ribbon, 95% CI. (**G**) Same as panel F for VPR, p65 and Rta, but stratified into cells with and without visible droplets (n = 13-40 cells per construct). Ribbon, 95% CI. For additional information about the experiments see **Tables S4** and **S5**.

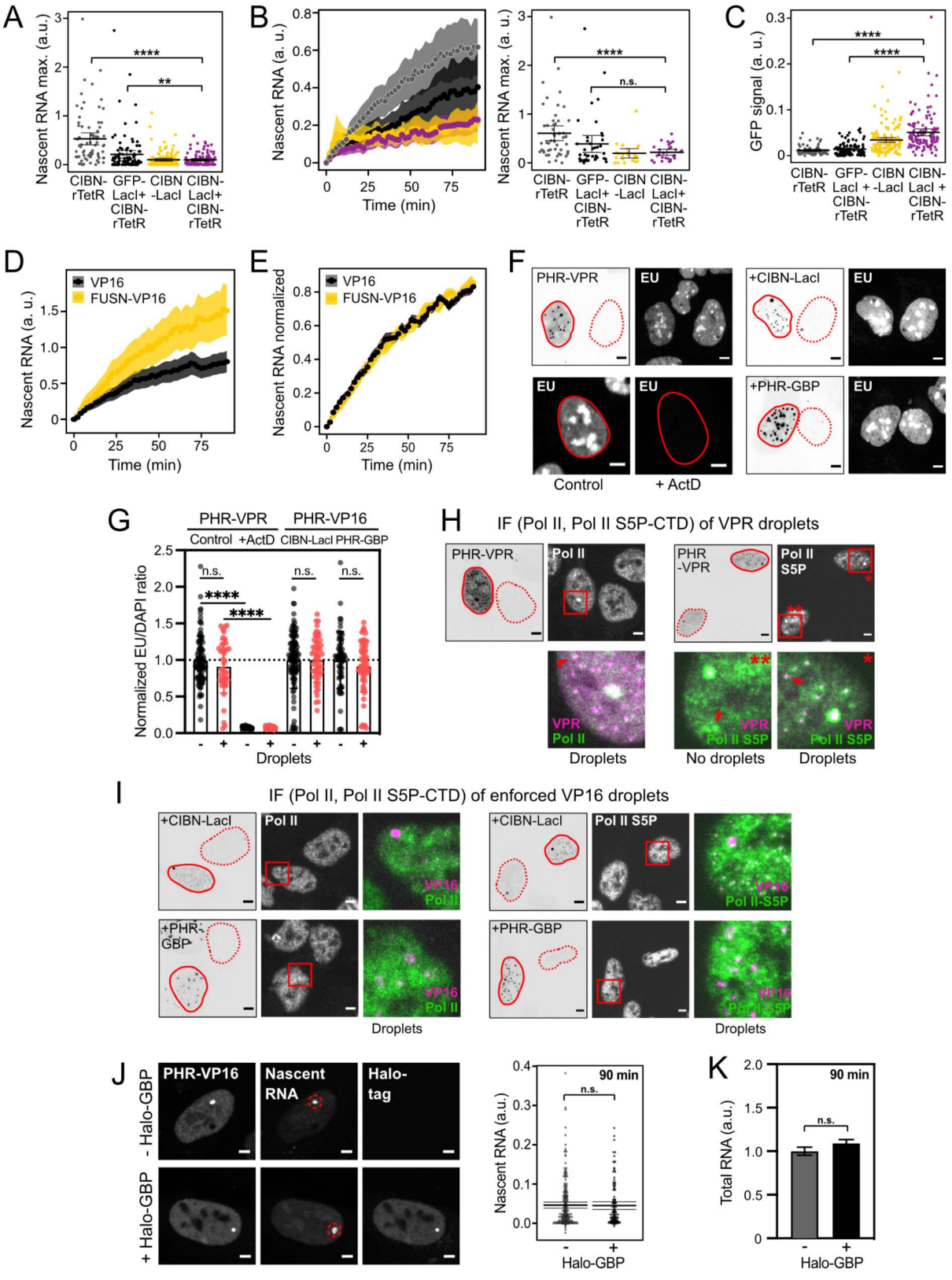

Figure S3. Control experiments for effects of droplet formation on transcription. Related to Fig. 4.

(**A**) Nascent RNA maximum plateau values for the data shown in **Figure 4E**. Two-sided Welch's t-test, p > 0.05, not significant (ns), $p < 0.01$ (**), $p < 0.0001$(****). (**B**) Averaged

nascent RNA time courses and maximum plateau values for activation in presence of CIBN-LacI induced droplets, responding cells only (*n* = 23-52 cells per condition, **Table S5**). Ribbon, 95% CI. (**C**) Quantified GFP signal at the reporter spot for the CIBN-LacI droplet induction experiment and control conditions (*n* = 74-126 cells per condition, **Table S5**). Two-sided Welch's t-test, $p < 0.0001$(****). (**D**) Same as **Figure 4I** but showing only the responding cells (*n* = 94-130 cells per condition, **Table S5**). Conditions FUSN and GBP+VP16 are not shown due to the low number of responding cells. (**E**) Average nascent RNA time courses normalized to maximum values of individual trajectories for comparison of activation kinetics of VP16 and FUSN-VP16 (*n* = 94-130, **Table S5**). Ribbon, 95% CI. (**F**) Representative images showing ethynyl-uridine (EU) pulse-labeling of global nascent RNA 90 min after activation/illumination, comparing cells with (solid outline) to cells without (dashed outline) visible droplets. The reporter gene cluster was activated using the rTetR-opto construct. The native droplet formation of PHR-VPR was compared to PHR-VP16 under conditions of droplet formation reinforced by bridging factors (+CIBN-LacI, +PHR-GBP, see **Figure 4A, B**). Actinomycin D treatment (2 µg/mL, 105 min) was used a positive control for transcription inhibition in cells expressing VPR recruited to rTetR-opto. Scale bars, 5 µm. (**G**) Quantification of the EU staining normalized to DAPI signal from panel F. For all conditions without ActD treatment, bright nucleolar EU signals were removed by segmentation before quantification. Bar depicts the mean and dots correspond to values from *n* = 41-103 single cells per condition (**Table S5**). Two-sided unpaired Student's t-test for indicated comparisons: $p>0.05$, not significant (n.s.), $p < 0.0001$ (****). (**H**) Representative images of cells with and without VPR for Pol II and Pol II S5P-CTD. Arrows highlight partial colocalization events of droplets with the IF signals. Note the granular Pol II S5P-CTD signal observed both in presence and absence of VPR droplets. Scale bars, 5 µm. (**I**) Same as panel H but for VP16. (**J**) Binding of non-bridging Halo-tag-GBP does not affect nascent steady-state RNA or total reporter RNA levels induced by PHR-VP16 after 90 min activation. Representative images of PHR-VP16, nascent RNA and Halo-tag-GBP. Scale bars, 5 µm. Bars: Mean and 95% CI of nascent RNA levels (*n* = 123 - 222 cells per condition, **Table S5**). Two-sided Welch's t-test, $p>0.05$; n.s., not significant. (**K**) Same as panel J but for quantification of total reporter RNA by qPCR. In the bar plot mean and s.d. (*n* = 3) values normalized to beta-actin mRNA are depicted without (-) and with (+) Halo-tag-GBP. Two-sided unpaired Student's t-test: $p>0.05$, not significant (n.s.).

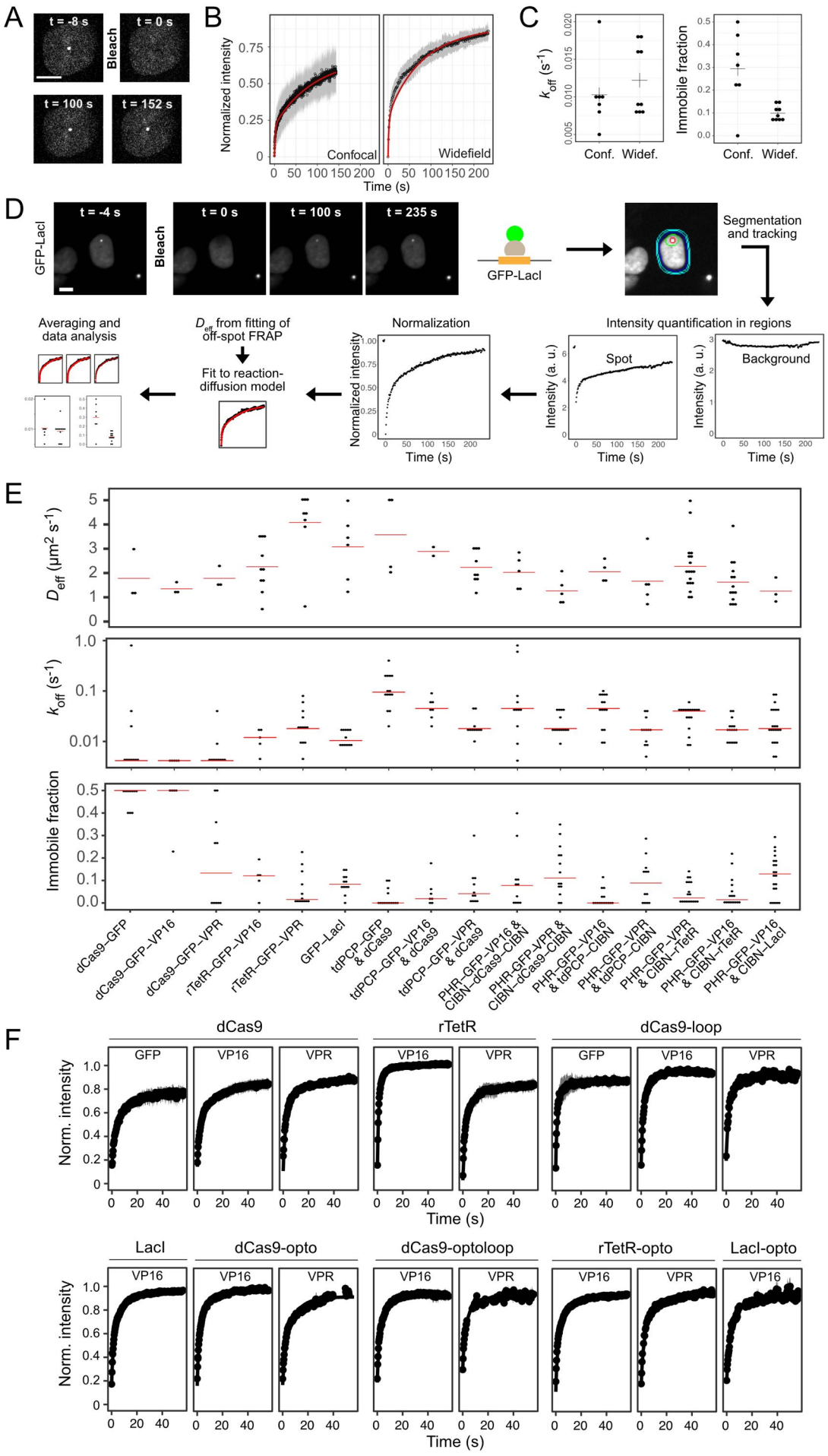
A
t = -8 s
Bleach
t = 0 s
t = 100 s
t = 152 s
B
Normalized intensity
Confocal
Widefield
Time (s)
C
k_{off} (s^{-1})
Immobile fraction
Conf.
Widef.
D
GFP-LacI
t = -4 s
Bleach
t = 0 s
t = 100 s
t = 235 s
GFP-LacI
Segmentation and tracking
Intensity quantification in regions
Spot
Background
Intensity (a. u.)
Time (s)
Normalization
Normalized intensity
D_{eff} from fitting of off-spot FRAP
Fit to reaction-diffusion model
Averaging and data analysis
E
D_{eff} (μm^2 s^{-1})
k_{off} (s^{-1})
Immobile fraction
dCas9–GFP
dCas9–GFP–VP16
dCas9–GFP–VPR
rTetR–GFP–VP16
rTetR–GFP–VPR
GFP–LacI
tdPCP–GFP & dCas9
tdPCP–GFP–VP16 & dCas9
tdPCP–GFP–VPR & dCas9
PHR–GFP–VP16 & CIBN–dCas9–CIBN
PHR–GFP–VPR & CIBN–dCas9–CIBN
PHR–GFP–VP16 & tdPCP–CIBN
PHR–GFP–VPR & tdPCP–CIBN
PHR–GFP–VPR & CIBN–rTetR
PHR–GFP–VP16 & CIBN–rTetR
PHR–GFP–VP16 & CIBN–LacI
F
dCas9
rTetR
dCas9-loop
GFP
VP16
VPR
Norm. intensity
Time (s)
LacI
dCas9-opto
dCas9-optoloop
rTetR-opto
LacI-opto

Figure S4. Experimental FRAP setup and data analysis. Related to Fig. 5.

(**A**) Image series of confocal FRAP of GFP-LacI bound to the reporter array. Scale bar, 10 µm. (**B**) Average recovery curves of GFP-LacI obtained by confocal and widefield FRAP. Ribbon, 95% CI; red line, fit of data to a reaction-diffusion model. The diffusive fraction is larger for widefield FRAP as discussed in the STAR Methods section. (**C**) Binding parameters of GFP-LacI fits in confocal (Conf.) and widefield (Widef.) mode. Red bar: median. (**D**) Image analysis workflow for widefield FRAP illustrated for GFP-LacI as an example. Scale bar, 10 µm. Automated segmentation and tracking of spot (red), local background region (green), nucleus (blue) and background around nucleus (cyan) over the time course was followed by intensity quantification in these regions. The spot intensity was normalized, and binding parameters were obtained by fitting a reaction-diffusion model, which uses the effective diffusion coefficient determined in off-spot FRAP experiments (**Table S6**). Normalized data, fit curves and fit parameters of single cells were averaged. (**E**) Distribution of parameters estimated from single cell recovery curves by a reaction-diffusion model. Effective diffusion coefficients were determined from off-spot FRAP while dissociation rate and immobile fraction were measured at the array. Red bar: median. (**F**) Average recovery curves for off-spot FRAP to determine the diffusion behavior of activation complexes. Fits of the data to a diffusion model are shown as solid line. Ribbon, 95% CI.

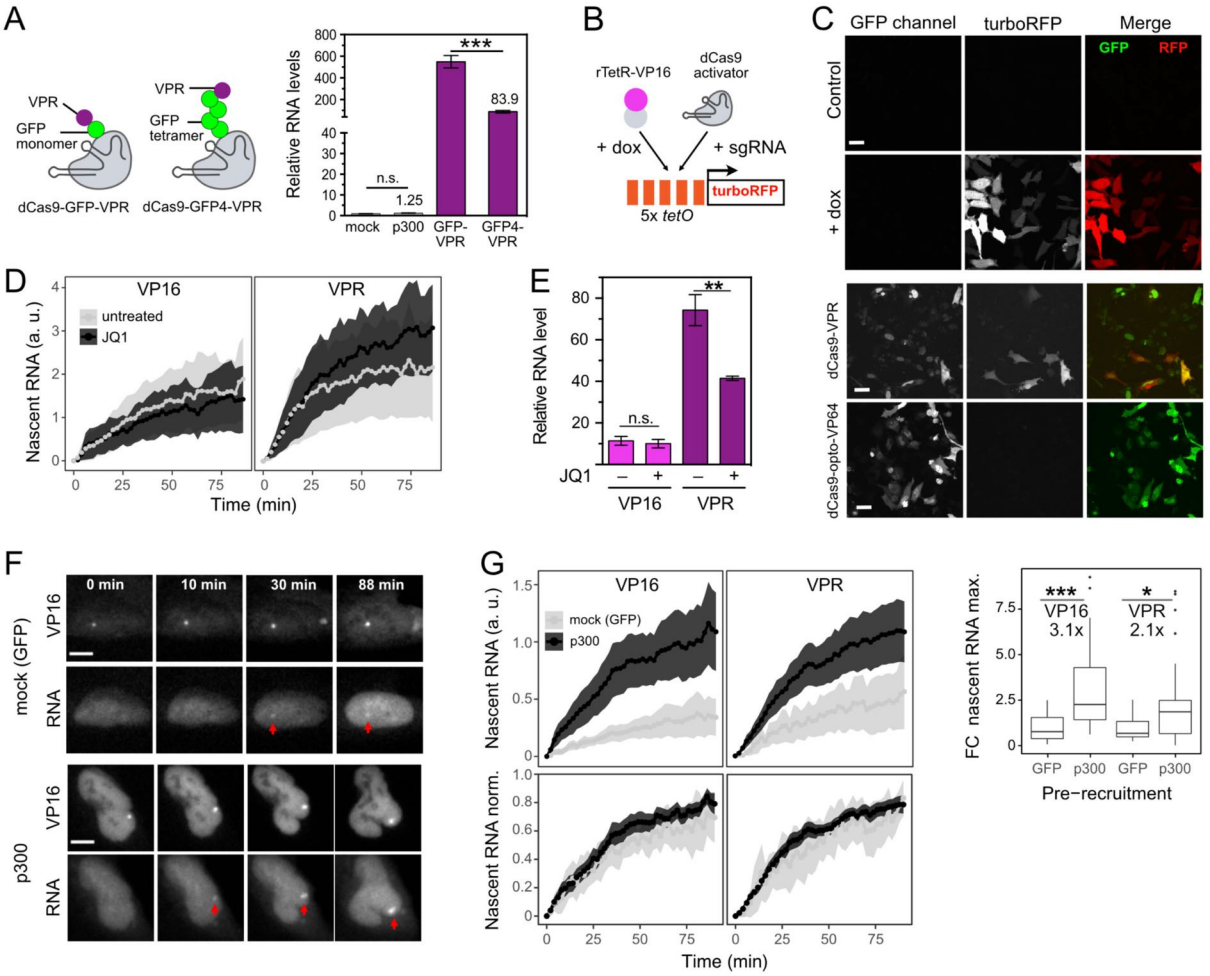

Figure S5. dCas9-opto/optoloop complexes, histone acetylation and BRD4 binding. Related to Fig. 6.

(**A**) Total reporter RNA levels (qPCR) measured for dCas9-VPR (from **Figure 6A**, shown for comparison) or dCas9-VPR with a tetrameric GFP spacer (dCas9-GFP4-VPR). The size of dCas9-GFP4-VPR is comparable to that of the dCas9-opto/optoloop complexes (~340 kDa). It had a reduced activity compared to the dCas9-GFP-VPR fusion but was still a strong activator (~84-fold reporter induction). dCas9-p300 was not sufficient to activate transcription of our reporter although it can activate certain single-copy genes (Hilton et al., 2015) including the *IL1RN* gene (Shrimp et al., 2018) that was also induced with CIBN-dCas9-CIBN (dCas9-opto) (Polstein and Gersbach, 2015). Mean fold changes and s.d. (n = 3) of reporter RNA levels were normalized to beta actin mRNA and are expressed relative to mock transfected cells. Two-sided unpaired Student's t-test: p>0.05, not significant (n.s.), $p < 0.05$ (*), $p < 0.001$ (***) (**B**) Experimental strategy for testing the activity of dCas9-opto constructs in the HeLa TRIPZ-ΔshRNA cell line. This cell line stably expresses rTetR-VP16 for induction of turboRFP expression upon doxycycline addition. The five *tet*O sites can be used for binding a dCas9 construct with a suitable sgRNA and analyze whether it can induce turboRFP. (**C**) Representative microscopy images of turboRFP expression in HeLa TRIPZ-ΔshRNA at 24 h after doxycycline addition (positive control), activation by dCas9-VPR or PHR-VP64

recruited via dCas9 in the dCas9-opto-VP64 construct, which has been characterized previously (Polstein and Gersbach, 2015). Both the addition of doxycycline and a targeted dCas9-VPR fusion induced the reporter after 24 hours. In contrast, dCas9-opto-VP64 failed to activate expression. Scale bar, 20 µm. (**D**) Averaged nascent RNA time courses for VP16 or VPR recruited via the rTetR-opto construct, with or without JQ1 pre-treatment (1 µM, 3 hours pre-induction). Mean values of normalized intensity and 95% CI are shown for n = 7-20 cells per condition (**Table S8**). (**E**) Total reporter RNA levels (qPCR) measured for the conditions depicted in panel D (90 min endpoint). Mean fold changes and s.d. (n = 3) of reporter RNA levels were normalized to beta actin mRNA and are expressed relative to mock transfected cells. Two-sided unpaired Student's t-test: p>0.05, not significant (n.s.), $p < 0.01$ (**), $p < 0.001$ (***). (**F**) Representative images series corresponding to the experiment depicted in **Figure 6I**, with VP16 as AD. VP16 was recruited via the rTetR-opto construct in cells with reporter acetylation pre-established by dCas-p300 (p300) or bound by dCas9 only (mock). Arrows indicate nascent RNA. Scale bars, 10 µm. (**G**) Nascent RNA time courses and maximum-normalized kinetics for the experiment shown in panel F, comparing the mock and acetylated/p300 condition for VP16 and VPR (n = 9-54 cells per condition, **Table S8**). Acetylation by p300 led to a 3.1-fold (VP16) or 2.1-fold (VPR) higher production of nascent RNA as shown in the box plot. Intensity values were normalized to the mean value of the respective mock condition. Two-sided Welch's t-test: $p < 0.05$ (*), $p < 0.001$ (***).

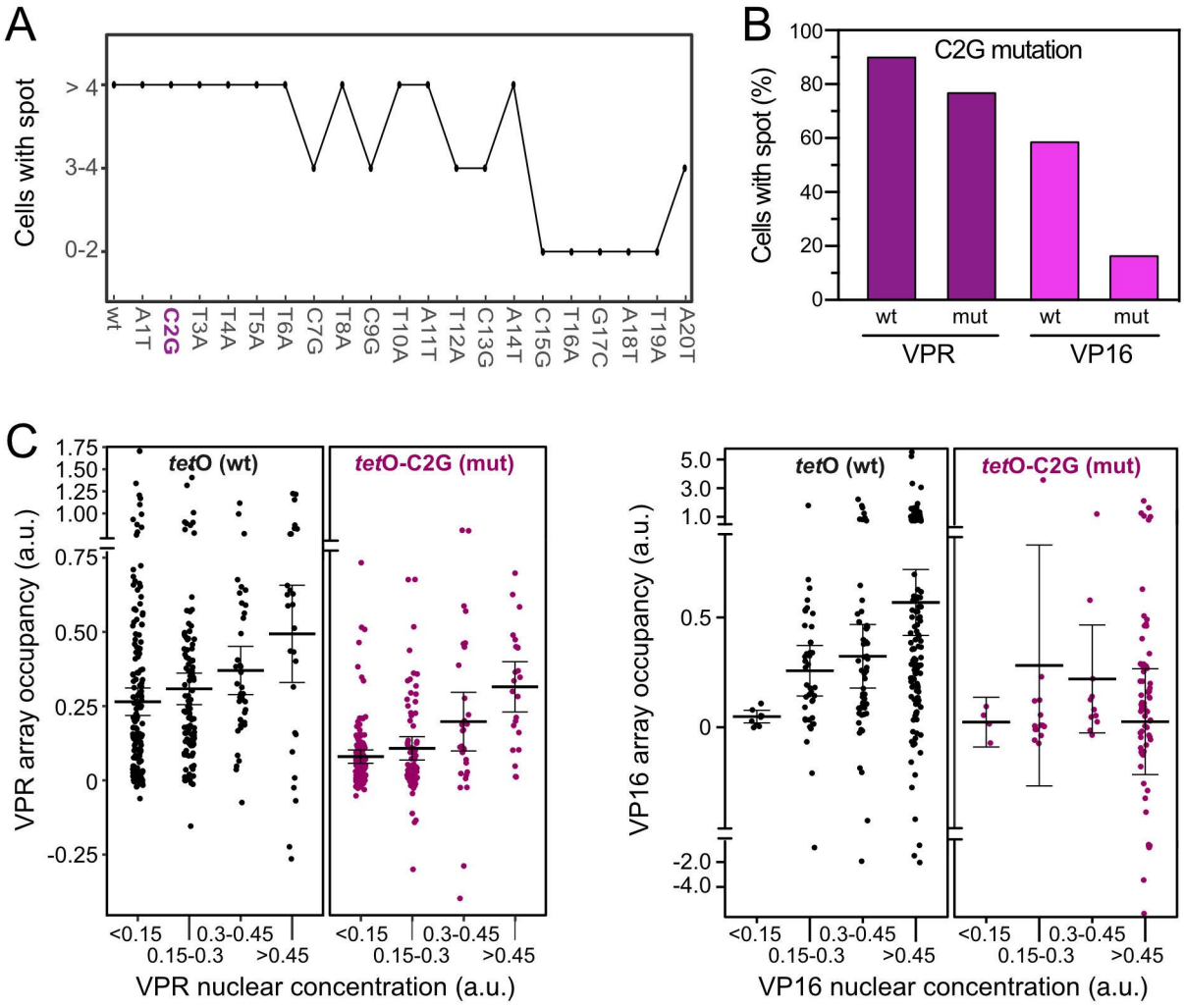

Figure S6. Modulation of TF residence time via sgRNA mutations. Related to Fig. 7.
(**A**) Screen of *tet*O-sgRNA mutations that reduced dCas9 binding while still enriching the construct at the reporter array. The mutations introduced into the sgRNA targeting region are depicted on the x-axis. dCas9-VPR was recruited to the reporter with a given sgRNA and the number of cells with visible reporter spot (GFP) was counted per field of view. (**B**) Fraction of cells with visible reporter array spots for dCas9-VPR or dCas9-VP16 recruited with sgRNA-wt or sgRNA-mut. A total of n = 127-175 cells were evaluated per condition. (**C**) Reporter array occupancy in dependence of the mutant sgRNA and the binned nuclear dCas9-VPR or dCas9-VP16 concentration (GFP fluorescence). Occupancy corresponds to the GFP spot intensity above background normalized to the co-transfected LacI array marker. Dots correspond to individual cells; mean and 95% CI error bars are indicated. Note the axis break to visualize all cells and outliers in one plot.

Supplemental Tables

Table S1. TF construct nomenclature. Related to Fig. 1.

TF name[a]	Constructs[a]
dCas9-AD	dCas9-GFP-AD + sgRNA_2xPP7
rTetR-AD	rTetR-GFP-AD
dCas9-loop-AD	dCas9 + tdPCP-GFP-AD + sgRNA_2xPP7
rTetR-opto-AD	CIBN-rTetR + PHR-GFP-AD
LacI-opto-AD	CIBN-LacI + PHR-GFP-AD
dCas9-opto-AD	CIBN-dCas9-CIBN + PHR-GFP-AD + sgRNA_2xPP7
dCas9-optoloop-AD	dCas9 + tdPCP-CIBN + PHR-GFP-AD + sgRNA_2xPP7

[a] AD refers to the activation domain VP16, VPR, p65, Rta or STAT2.

Table S2. Plasmid constructs. Related to Fig. 1.

Plasmid	Comment	Reference
rTetR-GFP	Tet-On transactivator, contains same NLS as VP16 constructs	This study
rTetR-GFP-VP16	VP16 domain from Addgene #103836	(Gunther et al., 2013), this study
rTetR-GFP-VPR	VPR domain from Addgene #63798	(Chavez et al., 2015), this study
CIBN-rTetR	CIBN domain of CIB1 from Addgene #26867 with T2A-Puro resistance.	(Kennedy et al., 2010), this study
GFP-LacI		(Jegou et al., 2009)
tagBFP-LacI	Addgene #103839	(Rademacher et al., 2017)
tdTomato-LacI	tdTomato from Addgene #54642	This study
CIBN-LacI	Addgene #103814	(Rademacher et al., 2017)
SNAPtag-LacI	LacI in pSNAPf vector	This study
dCas9	dCas9 from Addgene #60910 with HA-tag	This study
dCas9-GFP		(Erdel et al., 2020; Frank et al., 2021)
dCas9-GFP-VP16		This study
dCas9-GFP-VPR		(Erdel et al., 2020; Frank et al., 2021)
dCas9-GFP$_4$-VPR		This study
dCas9-GFP-p300	p300 core domain from Addgene #61357	This study
CIBN-dCas9-CIBN	Addgene #60553	(Polstein and Gersbach, 2015)
PHR-GFP	PHR domain of CRY2 from Addgene plasmid #26866, with NLS	(Kennedy et al., 2010; Rademacher et al., 2017)
PHR-GFP-VP16		This study
PHR-GFP-VPR		This study
PHR-GFP-p65	p65 domain from Addgene #63798	This study
PHR-GFP-Rta	Rta domain from Addgene #63798	This study
PHR-GFP-STAT2	STAT2 AD from	(Frahm et al., 2006), this study
PHR-GFP-FUSN	FUSN from Addgene #122148	(Bracha et al., 2018), this study
PHR-GFP-FUSN-VP16		(Bracha et al., 2018), this study
PHR-GBP	GBP from (Rothbauer et al., 2008)	This study
tdPCP-GFP	Tandem PCP from Addgene #40650	This study
tdPCP-GFP-VP16	TATA-box of the promoter removed	This study
tdPCP-GFP-VPR	TATA-box of the promoter removed	This study
tdPCP-CIBN	TATA-box of the promoter removed	This study
tdMCP-tdTomato	From Addgene #40649 and #54642 with TATA-box of the promoter removed	This study
mCherry-BRD4	mBRD4	(Rafalska-Metcalf et al., 2010), this study
Halo-tag-GBP	GBP in pHTN Halo-tag vector (Promega)	(Rothbauer et al., 2008), this study

Table S3. sgRNAs sequences used for dCas9 targeting. Related to Fig. 1 and 7.

sgRNA	Targeting sequence (5'-3')
tetO-2xPP7 (wt)	GACTTTTCTCTATCACTGATA
tetO-2xPP7-A1T	GTCTTTTCTCTATCACTGATA
tetO-2xPP7-C2G	GAGTTTTCTCTATCACTGATA
tetO-2xPP7-T3A	GACATTTCTCTATCACTGATA
tetO-2xPP7-T4A	GACTATTCTCTATCACTGATA
tetO-2xPP7-T5A	GACTTATCTCTATCACTGATA
tetO-2xPP7-T6A	GACTTTACTCTATCACTGATA
tetO-2xPP7-C7G	GACTTTTGTCTATCACTGATA
tetO-2xPP7-T8A	GACTTTTCACTATCACTGATA
tetO-2xPP7-C9G	GACTTTTCTGTATCACTGATA
tetO-2xPP7-T10A	GACTTTTCTCAATCACTGATA
tetO-2xPP7-A11T	GACTTTTCTCTTTCACTGATA
tetO-2xPP7-T12A	GACTTTTCTCTAACACTGATA
tetO-2xPP7-C13G	GACTTTTCTCTATGACTGATA
tetO-2xPP7-A14T	GACTTTTCTCTATCTCTGATA
tetO-2xPP7-C15G	GACTTTTCTCTATCAGTGATA
tetO-2xPP7-T16A	GACTTTTCTCTATCACAGATA
tetO-2xPP7-G17C	GACTTTTCTCTATCACTCATA
tetO-2xPP7-A18T	GACTTTTCTCTATCACTGTTA
tetO-2xPP7-T19A	GACTTTTCTCTATCACTGAAA
tetO-2xPP7-A20T	GACTTTTCTCTATCACTGATT
lacO-2xPP7 (wt)	GTCCGCTCACAATTCCACATG
tetO-turboRFPreporter-2xPP7	GATACGTTCTCTATCACTGAT

All sgRNAs were cloned into the U6 promoter-driven sgRNA expression vector originally derived from Addgene #61424 and engineered to contain two PP7 stem loops PP7. The PP7 loop sequence was adapted from ref. (Zalatan et al., 2015).

Table S4. Propensity of the activation domain to form optodroplets. Related to Fig. 1 and S2.

PHR-GFP-AD	DNA binder	Cell number	Droplets (%)[a]	c_{crit} (a. u.) [b]
VP16	CIBN-rTetR	131	29	0.54
VPR	CIBN-rTetR	38	86	0.19
p65	CIBN-rTetR	129	72	0.28
Rta	CIBN-rTetR	34	41	0.33
STAT2	CIBN-rTetR	103	0	>1.5 [c]
VP16	CIBN-LacI	79	56	0.34
VPR	CIBN-LacI	106	63	0.23

Cells were classified as positive for droplet formation if they displayed nuclear optodroplets in microscopy images in addition to the signal at the reporter array (**Figure 1C**).

[a] The percentage of cells with droplets depends on the nuclear concentration range for each construct, but allows a simple distinction between droplet-forming and non-droplet-forming ADs at typical expression levels.

[b] The critical value for droplet formation c_{crit} was determined from the relation of nuclear PHR-GFP-AD concentration and droplet abundance shown in **Figure 1D** and **Figure S2A**.

[c] If droplet abundance did not exceed the threshold value within the measured nuclear concentrations the critical concentration is reported as greater than the highest observed nuclear concentration.

Table S5. Transcription activation kinetics. Related to Fig. 3, 4, S2 and S3.

PHR-GFP-AD	Condition	Cell number	Responders (%)	$t_{1/2}$ (min) [a]	Maximum RNA value (a. u.) [a]
VP16	All cells	64	67	42 (37-46)	1.2 (0.89-1.6)
VPR	All cells	37	84	28 (23-33)	1.7 (1.1-2.4)
VPR	Cells without droplets	15	87	25 (17-34)	1.1 (0.83-1.4)
VPR	Cell with droplets	22	82	30 (24-36)	2.2 (1.0-3.3)
p65	All cells	52	67	26 (21-31)	2.1 (1.6-2.6)
p65	Cells without droplets	23	78	26 (19-33)	2.3 (1.5-3.0)
p65	Cell with droplets	29	59	26 (18-34)	1.9 (1.2-2.7)
Rta	All cells	77	92	28 (25-31)	1.2 (0.92-1.5)
Rta	Cells without droplets	33	94	25 (21-29)	1.2 (0.73-1.7)
Rta	Cell with droplets	44	91	31 (26-36)	1.2 (0.85-1.6)
STAT2	All cells	132	42	38 (34-43)	0.95 (0.66-1.2)
Reinforced droplet experiments					
VP16	No additional factors	74	70	35 (30-39)	0.61 (0.46-0.76)
VP16	GFP-LacI	97	42	34 (28-39)	0.39 (0.22-0.56)
VP16	CIBN-LacI	118	24	31 (23-38)	0.22 (0.16-0.28)
VP16	CIBN-LacI but no CIBN-rTetR	126	18	20 (13-28)	0.20 (0.09-0.29)
VP16	No additional factors	154	84	34 (31-36)	0.78 (0.63-0.93)
VP16	PHR-GBP	24	4	n. d. [b]	n. d. [b]
FUS-VP16	No additional factors	108	87	37 (34-41)	1.5 (1.1-1.8)
FUS	No additional factors	57	5	n. d. [b]	n. d. [b]

The RNA production at the reporter gene cluster was followed over time via the tdMCP-tdTomato signal. rTetR-opto was used as DBD module unless stated otherwise.

[a] The maximum of RNA produced was determined from the last five time points at the plateau of the single cell time course, and the time $t_{1/2}$ was determined where half of this values was reached. Mean values and 95% CIs were calculated from the analysis of responding cells that showed an RNA signal at the reporter array. Data for VP16 and p65 as well as for VPR, Rta and STAT2 were acquired together. A direct comparison of VPR and VP16 done in other experiments yielded a VPR/VP16 ratio of maximum activation values of ~1.5 after 90 minutes.

[b] Values could not be determined due to the low number of responder cells.

Table S6. FRAP parameters from reaction-diffusion analysis. Related to Fig. 5 and S4.

Protein(s)	DNA	D_{eff} (μm²/s)	Diffusive fract. (%)	Residence time t_{res} (s)	Bound fract. (%)	Immobile fract. (%)	*n*
GFP-LacI	*lac*O	2.3 (1.5-3.0)	29 (21-37)	82 (63-115)	61 (53-69)	10 (7-12)	9
GFP-LacI (confocal)[a]	*lac*O	3.3 (2.0-4.5)	22 (5-38)	97 (68-167)	49 (38-60)	29 (14-45)	7
dCas9-GFP	*lac*O	1.8 (0-4.3)	34 (29-40)	n.d.[b]	19 (14-24)	47 (44-50)	10
dCas9-GFP-VP16	*lac*O	1.4 (0.8-2.0)	28 (11-45)	n.d.[b]	27 (14-41)	45 (30-60)	5
dCas9-GFP-VPR	*lac*O	1.8 (0.7-2.9)	36 (27-44)	121 (61-n.d.)[b]	46 (34-57)	19 (4-34)	10
dCas9-GFP-VPR	*tet*O	0.6 (0.4-0.9)	41 (35-47)	83 (47-n.d.)[b]	25 (16-33)	34 (22-47)	9
dCas9-GFP-VPR	*tet*O-C2G	0.6[d]	48 (34-62)	48 (32-94)	45 (30-60)	7 (0-16)	7
rTetR-GFP-VP16	*tet*O	4.3 (3.0-5.4)	57 (42-71)	84 (54-193)	32 (17-48)	11 (2-20)	5
rTetR-GFP-VPR	*tet*O	3.1 (1.6-4.5)	36 (28-44)	39 (26-80)	59 (50-67)	5 (1-10)	12
dCas9 + tdPCP-GFP	*lac*O	3.4 (0.9-6.2)	29 (20-38)	8 (5-13)	69 (60-78)	2 (0-4)	14
dCas9 + tdPCP-GFP-VP16	*lac*O	2.9 (0.6-5.2)	46 (35-58)	20 (14-36)	49 (37-61)	5 (0-10)	7
dCas9 + tdPCP-GFP-VPR	*lac*O	2.2 (1.7-2.8)	15 (10-20)	46 (34-73)	78 (71-86)	7 (1-12)	11
CIBN-dCas9-CIBN + PHR-GFP-VP16	*lac*O	2.0 (1.2-2.9)	41 (36-46)	6 (3-n.d.)[b]	49 (42-55)	10 (1-19)	11
CIBN-dCas9-CIBN + PHR-GFP-VPR	*lac*O	1.3 (0.6-1.9)	28 (24-34)	41 (32-57)	57 (51-64)	14 (8-21)	14
dCas9 + tdPCP-CIBN + PHR-GFP-VP16	*lac*O	2.1 (1.4-2.8)	44 (35-54)	19 (14-28)	54 (45-63)	2 (0-4)	14
dCas9 + tdPCP-CIBN PHR-GFP-VPR	*lac*O	1.7 (0.4-3.0)	21 (17-25)	53 (38-87)	69 (62-77)	10 (3-16)	12
CIBN-rTetR + PHR-GFP-VP16	*tet*O	2.3 (1.7-2.8)	42 (37-47)	29 (24-36)	54 (48-59)	4 (2-7)	17
CIBN-rTetR + PHR-GFP-VPR	*tet*O	1.6 (1.1-2.1)	25 (19-31)	53 (42-75)	70 (64-77)	5 (1-8)	16

Measurements were conducted with the widefield microscopy setup except for the indicated measurement of GFP-LacI. As described in the STAR Methods a reaction-diffusion analysis of clustered binding sites was conducted to determine mean values and 95% confidence intervals for three molecular species characterized by (i) the effective diffusion coefficient D_{eff}, (ii) binding with residence time $t_{res} = 1/k_{off}$ and (iii) the fraction of immobile molecules.

[a] Values are expected to differ from the corresponding value in the widefield setup since less freely diffusing fluorescent particles above and below the array are visible in a confocal setup. For further details see STAR Methods.

[b] Values exceeding the observation time period of 240 sec could be not reliably determined.

[c] For fitting of the diffusion-binding model to the data the D_{eff} value for dCas9-GFP-VPR with *tet*O-sgRNA(wt) was used.

Table S7. Reporter RNA expression measured by qRT-PCR. Related to Fig. 6, 7 and S5.

DNA binder	AD	Treatment	RNA fold-change
– (mock transfection, reference for normalization)	–	24 h light	1.0
– (untransfected)	–	24 h light	0.9
dCas9-GFP-VP16	VP16 (fusion)	24 h light	6.4
dCas9-GFP-VPR	VPR (fusion)	24 h light	550
dCas9-GFP$_4$-VPR	VPR (fusion)	24 h light	84
dCas9-GFP-VP16 (tetO-C2G)	VP16 (fusion)	24 h light	0.9
dCas9-GFP-VPR (tetO-C2G)	VPR (fusion)	24 h light	31
dCas9-GFP-p300	p300 (fusion)	24 h light	1.3
rTetR-GFP-VP16	VP16 (fusion)	24 h light + dox	35
rTetR-GFP-VPR	VPR (fusion)	24 h light + dox	217
dCas9 (tetO-PP7)	tdPCP-GFP-VP16	24 h light	4.0
dCas9 (tetO-PP7)	tdPCP-GFP-VPR	24 h light	490
CIBN-dCas9-CIBN	PHR-GFP-VP16	24 h light	1.7
CIBN-dCas9-CIBN	PHR-GFP-VPR	24 h light	1.8
CIBN-dCas9-CIBN	PHR-GFP-VP16	dark	1.3
CIBN-dCas9-CIBN	PHR-GFP-VPR	dark	1.6
dCas9 + tdPCP-CIBN	PHR-GFP-VP16	24 h light	1.0
dCas9 + tdPCP-CIBN	PHR-GFP-VPR	24 h light	1.4
CIBN-rTetR	PHR-GFP-VP16	dox, 24 h light	32
CIBN-rTetR	PHR-GFP-VPR	dox, 24 h light	17.5
CIBN-rTetR + CIBN-LacI	PHR-GFP-VP16	dox, 90 min light	3.1
CIBN-rTetR + GFP-LacI	PHR-GFP-VP16	dox, 90 min light	5.3
CIBN-LacI	PHR-GFP-VP16	dox, 90 min light	1.7
CIBN-rTetR	PHR-GFP-VP16	dox, 90 min light	7.0
CIBN-rTetR	PHR-GFP-FUSN	dox, 90 min light	1.8
CIBN-rTetR	PHR-GFP-FUSN-VP16	dox, 90 min light	70
CIBN-rTetR	PHR-GFP-VP16 + PHR-GBP	dox, 90 min light	1.9
CIBN-rTetR [a]	PHR-GFP-VP16	dox, untreated, 90 min light	11
CIBN-rTetR [a]	PHR-GFP-VPR	dox, untreated, 90 min light	74
CIBN-rTetR [b]	PHR-GFP-VP16	dox, 3 h JQ1, 90 min light	10
CIBN-rTetR [b]	PHR-GFP-VPR	dox, 3 h JQ1, 90 min light	41
CIBN-rTetR [c]	PHR-GFP-VP16	dCas9-GFP *lac*O, dox, 90 min light	9.7
CIBN-rTetR [c]	PHR-GFP-VPR	dCas9-GFP *lac*O, dox, 90 min light	111
CIBN-rTetR [c]	PHR-GFP-VP16	dCas9-GFP-p300 *lac*O + dox, 90 min light	15
CIBN-rTetR [c]	PHR-GFP-VPR	dCas9-GFP-p300 *lac*O + dox, 90 min light	95

Doxycycline (dox) was added directly after transfection and cells were illuminated for 24h for the “24h light” experiments. For the “90 min light” condition, dox was added 24h after transfection; cells were exposed to light after 15 min for 90 min. JQ1 treatment started 3 h before the start of illumination. RNA levels were normalized to beta actin mRNA for each

sample and fold-changes were determined from the average of three measurements relative to the mock transfected cells.

[a] Reference for the JQ1 treatment experiment.

[b] Cells were treated with JQ1 at a 1 μM concentration in the dark for 3 h and then activated with light.

[c] Local hyperacetylation was induced by recruiting dCas9-p300 with the *lac*O sgRNA for 24 h.

Table S8. Histone acetylation, BRD4 binding and transcription activation. Related to Fig. 6 and S5.

DNA binder and readout	AD	Condition	Cell number	Responders (%)	$t_{1/2}$ (min)	Maximum value (a. u.) [a]
dCas9-optoloop, mCherry-BRD4	VP16	–	37	27	13 (7-20)	0.007 (0.005-0.010)
		JQ1	85	0	–	0.002 (0.002-0.003)
	VPR	–	13	92	13 (8-18)	0.024 (0.016-0.032)
		JQ1	10	10	–	0.005 (0.002-0.008)
rTetR-opto, tdMCP-tdTomato (RNA)	VP16	–	29	69	35 (30-39)	1.7 (0.91-2.5)
		JQ1	12	58	28 (18-39)	1.4 (0.63-2.2)
	VPR	–	15	87	29 (20-39)	2.1 (1.0-3.2)
		JQ1	21	81	33 (27-38)	3.0 (2.0-4.0)
	VP16	dCas9-GFP	52	25	35 (25-44)	0.35 (0.18-0.51)
		dCas9-GFP-p300	49	53	31 (27-36)	1.1 (0.76-1.4)
	VPR	dCas9-GFP	27	33	37 (19-54)	0.51 (0.23-0.79)
		dCas9-GFP-p300	72	75	31 (27-34)	1.1 (0.82-1.4)

Transcription activation time course parameters were determined as described for **Table S5**.

[a] Maximum values for RNA production can be compared directly only for the same DNA binding module and experimental conditions. For the experiments with BRD4, values are given for the whole population of responding and non-responding cells due to the low number of responding cells detected after JQ1 treatment.

Table S9. Binding site occupancy of dCas9. Related to Fig. 5 and 7.

Complex	AD	sgRNA	Occupancy [a]	Number of cells	Visible array (%) [b]
dCas9-loop	VP16	*tet*O-2xPP7 (wt)	0.53 (0.41-0.66)	166	78
dCas9-loop	VPR	*tet*O-2xPP7 (wt)	0.99 (0.77-1.22)	164	93
dCas9-VP16	VP16 (fusion)	*tet*O-2xPP7 (wt)	0.24 (0.17-0.30)	138	59
		*tet*O-2xPP7-C2G (mut)	0.03 (0.01-0.06)	127	17
dCas9-VPR	VPR (fusion)	*tet*O-2xPP7 (wt)	0.32 (0.26-0.37)	175	90
		*tet*O-2xPP7-C2G (mut)	0.12 (0.09-0.14)	163	76

Binding site occupancy at the reporter array were determined as the ratio of the GFP fluorescence of the activator complex and the blue fluorescence signal of tagBFP-LacI as an array marker.

[a] Mean value and 95% CI. Data can be directly compared only for experiments conducted with the same DNA binding module.

[b] Fraction of cells that had the activator complex GFP signal enriched at the site of the array marked by tagBFP-LacI.